
FDTD Simulation von Elektronenstreuung an einer elektromagnetischen Welle

FDTD Simulation of electron scattering in an electromagnetic wave

David Symhoven



München 2017

FDTD Simulation von Elektronenstreuung an einer elektromagnetischen Welle

FDTD Simulation of electron scattering in an electromagnetic wave

David Symhoven

Masterarbeit
am Lehrstuhl Computational & Plasma Physics
der Ludwig-Maximilians-Universität
München

vorgelegt von
David Symhoven
aus Witten

München, den 18.07.2017

Gutachter: Prof.Dr. Hartmut Ruhl

Introduction

With the increase of computational power over the last decade computer simulations became more and more attractive. Not just that it allows us to work with circumstances which are nearly impossible to create in the lab, it can also be used to make fundamental physics visible or understand the consequences of fundamental physical laws. We can use simulations to help interpret experiments or even help designing new ones. Simulations can provide detailed information about patterns and behaviors we - as humans - could never see in reality. For instance, on subatomic scales dynamics and their consequences are way too fast for us to see, like the radiation of relativistic electrons.

A computer simulation of N interacting particles can be conducted by solving Newton's equation for each particle in the system. This is called *particle-particle* approach. The main cost of computational power is the calculation of the force \vec{F} acting on a particle. This requires a summation over all other particles in the system

$$\vec{F} = \sum_{i,j} \vec{F}_{ij},$$

where \vec{F}_{ij} is the interaction force of particle i with particle j . Once the force is calculated, the underlying equation of motion can be used to calculate the velocity at a new time step and with that the new position of the particle. With the new position, the forces need to be updated and the cycle starts over. For each particle there are $N - 1$ other particles to interact with. Considering that each pair interaction only needs to be calculated once, this results in a total of $\frac{N(N-1)}{2}$ calculations. For strongly coupled systems, where the number of particles is usually small compared to weakly coupled systems, this approach is feasible. For weakly coupled systems, however, where one usually has more than 10^8 particles, the computational costs become too high. Even the more efficient *Barnes-Hut* or *tree* algorithm [2] which has numeric complexity of $\mathcal{O}(N \log(N))$ is not sufficient. This is where the *Particle-in-Cell* (PIC) algorithm comes in.

PIC is the standard simulation framework for Plasma Physics today. It was *Bunemann, Dawson, Hockney, Birdsall* and *Langdon* who promoted the development of PIC the most in the 1950's and 60's [6, 8, 9]. Whereas first simulations were limited by computational power to one dimensional problems, nowadays even three dimensional simulations are

feasible [4, 11, 16].

For instance, a modern super computer can achieve 100 TFLOP/s. A common simulation with 10^8 particles for 10000 time steps would require about three years. The same simulation using PIC with $64 \times 64 \times 64$ cells only requires three seconds [18].

Christian Herzing developed in his PhD-thesis an hybrid field approach to improve PIC even further [12]. By introducing near and far fields he could reduce the numeric complexity to almost $\mathcal{O}(N)$. His framework is written in C++. Unfortunately this is not compatible with the *Leibnitz-Rechenzentrum* (lrz) infrastructure, which requires C code input. So, the goal of this work is first to translate the framework into C and second, to build a solid and well documented code base others can build upon. To show that the framework is applicable, a real world use case, that is the scattering of an electron in a electromagnetic wave - is simulated.

The thesis is structured in three parts. The first part deals with the fundamentals. We present the steps of how to derive the inhomogeneous wave equation with the help of the potential equations and solve it afterwards using greens function approach.

In the second part the necessary numeric background is presented. We will present the underlying equations of motion and how to solve them numerically. Thereto several integration schemes are presented. We then continue to explain the hybrid field approach from Christian Herzing and the *Finite Difference Time Domain* (FDTD) method, which is used to solve Maxwell Equations on a discretized grid. We then close the second part with the theory and implementation of „Uniaxial Perfectly Matched Layer“ which deals with the behavior of incident waves at the simulation boundary.

A summary and outlook is given in the third part.

Lastly, there is also an Appendix where some additional calculations and topics like normalization and the used software stack are covered.

Acknowledgments

The last ten month have been a great time for me. Both challenging and exhausting but great and exciting. In my opinion we should soften the distinction between the different departments even further. Interdisciplinarity becomes more and more important as the complexity of modern research increases. Computational physics requires good software engineering. Likewise, Software Engineers can benefit from the knowledge of physicists or mathematicians. This is the reason why I liked the idea of writing a simulation framework so much. Although it's not a common thing to do in a physics master thesis, I learned a lot about programming. I really want to thank you - Prof. Ruhl - for sharing this opinion with me and for giving me the opportunity to write this thesis and of course for your input all along the way. It was always fun and inspiring to discuss with you about physics and non-physics related topics like climate change, electro mobility and the education system, just to mention a few.

Especially the last three month have been hard, because I already started my regular job in April. Thanks for your understanding and support!

Also big thanks to Ute Tobiasch for your reliability and scheduling all the appointments. Thanks to my friends XX and XX for proofreading.

Finally I want to thank my colleagues Julian Manke and Manuel Linder whom I shared an office with. Thanks for your support, the long discussions and your help!

Symbols and Constants

Vacuum permittivity	ϵ_0	$8.85418781762 \cdot 10^{-12} \text{ As V}^{-1} \text{ m}^{-1}$
Vacuum permeability	μ_0	$2566370614 \cdot 10^{-6} \text{ N A}^{-2}$
Speed of Light	c	$299792458 \text{ m s}^{-1}$
Electron charge	q	$1.6021766208 \cdot 10^{-19} \text{ C}$
Electron mass	m_e	$9.10938356 \cdot 10^{-31} \text{ kg}$
Electrical flux density	\vec{D}	$[\text{A s m}^{-2}]$
Magnetic flux density	\vec{B}	$[\text{T}]$
Magnetic field strength	\vec{H}	$[\text{A m}^{-1}]$
Electric field strength	\vec{E}	$[\text{V m}^{-1}]$
Electromagnetic Field Tensor	F_ν^μ	
Poynting Vector	\vec{S}	$[\text{N m}^{-1} \text{ s}^{-1}]$
Position	\vec{r}	$[\text{m}]$
Velocity	\vec{v}	$[\text{m s}^{-1}]$
Normalized Velocity	$\vec{\beta} = \frac{\vec{v}}{c}$	$[]$
Normalized Acceleration	$\dot{\vec{\beta}}$	$[\text{s}^{-1}]$
Wavelength	λ	$[\text{m}]$
Wavevector	\vec{k}	$[\text{m}^{-1}]$
Force	\vec{F}	$[\text{N}]$
Mass	m	$[\text{kg}]$
Energy	E	$[\text{J}]$
Power	W	$[\text{W}]$
Time	t	$[\text{s}]$
discretized Time	h	$[\text{s}]$
Frequenzy	ω	$[\text{s}^{-1}]$
Nabla - Operator	$\vec{\nabla}$	$\left(\frac{\partial}{\partial r_1}, \dots, \frac{\partial}{\partial r_n} \right)$
Laplace - Operator	Δ	$\sum_{i=1}^n \frac{\partial^2}{\partial r_i^2}$
d'Alembert - Operator	$\hat{\square}$	$\Delta - \frac{1}{c^2} \frac{\partial^2}{\partial t^2}$

Contents

Acknowledgments	vii
I. Fundamentals	2
1. Electromagnetic radiation	4
1.1. Maxwell-Equations	4
1.2. Colomrb and Lorentz Gauge	5
1.3. Liénard-Wiechert Potentials	6
1.3.1. Solution of the inhomogeneous wave equation	6
1.3.2. Special Case: Moving point charge	7
1.3.3. Energy emission	10
II. Numerics	14
2. Integration of Equation of Motion	16
2.1. Equations of Motion	16
2.2. Euler-Scheme	17
2.2.1. Procedural Error and Order of Consistency	18
2.3. Leap-Frog-Scheme	20
2.3.1. Boris-Method	21
3. Interpolations	24
3.1. Linear interpolation of Trajectories	24
3.2. Trilinear Interpolation of Fields	26
4. Hybrid Field Approach	28
4.1. FDTD	28
4.2. Numeric Dispersion Relation	30
4.3. Near-and Far Fields	33

CONTENTS

4.4.	Field Push	34
4.4.1.	pushEFieldInsideBoxes()	38
4.4.2.	setHFieldOnBorders()	38
4.4.3.	adjustHField()	38
4.4.4.	pushEFieldOnBorders()	38
4.5.	Particle Push and Near Field Update	40
4.6.	Particle History	42
4.7.	Far Field Setup Before Simulation	44
4.8.	Electron Scattering in an electromagnetic wave	47
5.	Uniaxial Perfectly Matched Layer	63
5.1.	Introduction	63
5.2.	Derivation	64
5.3.	Update Equations	68
5.4.	Implementation of UPML in FDTD	70
III.	Summary	72
IV.	Appendix	73
A.	Gauge Transformations	74
A.1.	Invariance of Fields	74
A.2.	Invariance of Potential Equations	75
B.	Retarded Potential Equations Fulfill Laurentz Gauge	76
C.	Softwarestack and Documentation	78
D.	Normalization	79
	Bibliography	84
	Declaration	87

Part I.

Fundamentals

In this first part we present the theoretical basics this thesis is build upon. We start with the foundation of electromagnetism - the Maxwell Equations - followed by the corresponding potential equations. Introducing Lorentz-Gauge will lead us to the inhomogeneous wave equation, which we will solve using Greens-function approach. This will lead us to the Liénard-Wiechert potentials, which are key for this thesis. Lastly, we discuss both, the non relativistic and relativistic phenomenon of energy radiation, where we restrict ourselves to the simple case where a particle is accelerated parallel to its direction of motion.

Electromagnetic radiation

1.1 Maxwell-Equations

The Maxwell equations are the foundation of the classical electromagnetism theory. They describe how the electric field strength $\vec{E} \in \mathbb{R}^3$ and the magnetic field strength $\vec{H} \in \mathbb{R}^3$ are generated by charges and currents respectively and how they evolve over time in space in presence of one another. In presence of matter, however, the interaction of the fields with the material need to be taken into account. The effect of microscopic dipoles, formed by bound charge carriers, are summarized in macroscopic entities called Polarisation $\vec{P} \in \mathbb{R}^3$ and Magnetization $\vec{M} \in \mathbb{R}^3$. These dipoles align in the external field such that the resulting electric and magnetic field are described by

$$\begin{aligned}\vec{D} &:= \epsilon_0 \vec{E} + \vec{P} \\ \vec{H} &:= \frac{1}{\mu_0} \vec{B} - \vec{M},\end{aligned}\tag{1.1}$$

where μ_0 and ϵ_0 are the vacuum permeability and permittivity respectively. The macroscopic Maxwell Equations than read

$$\vec{\nabla} \cdot \vec{B} = 0\tag{1.2}$$

$$\vec{\nabla} \cdot \vec{D} = \rho\tag{1.3}$$

$$\vec{\nabla} \times \vec{E} = -\frac{\partial \vec{B}}{\partial t}\tag{1.4}$$

$$\vec{\nabla} \times \vec{H} = \frac{\partial \vec{D}}{\partial t} + \vec{j},\tag{1.5}$$

where ρ denotes the charge density of the electric source and \vec{j} the electric current density. In the case of vacuum, the material equations (1.1) reduce to

$$\begin{aligned}\vec{D} &= \epsilon_0 \vec{E} \\ \vec{H} &= \frac{1}{\mu_0} \vec{B}.\end{aligned}\tag{1.6}$$

1.2 Colom and Lorentz Gauge

In the following section we consider the Maxwell Equations in vacuum. The electric and magnetic fields can also be described by a scalar and a vector potential respectively. From (1.2) we can conclude that

$$\exists \vec{A} \in \mathbb{R}^3 : \vec{B} = \vec{\nabla} \times \vec{A}, \quad (1.7)$$

where \vec{A} is called the vector potential. Plugging in (1.7) into (1.4) yields

$$\begin{aligned} \vec{\nabla} \times \left(\vec{E} + \frac{\partial \vec{A}}{\partial t} \right) &= 0. \\ \Rightarrow \exists \varphi \in \mathbb{R} : \vec{E} + \frac{\partial \vec{A}}{\partial t} &= -\vec{\nabla} \varphi. \end{aligned} \quad (1.8)$$

φ is called scalar potential. Plugging in (1.8) into (1.3) and also (1.7) and (1.8) into (1.5) gives the potential equations

$$\begin{aligned} -\Delta \varphi - \vec{\nabla} \left(\frac{\partial \vec{A}}{\partial t} \right) &= \frac{\rho}{\epsilon_0} \\ \underbrace{\left(\Delta - \frac{1}{c^2} \frac{\partial^2}{\partial t^2} \right)}_{:= \hat{\square}} \vec{A} - \vec{\nabla} \left(\vec{\nabla} \vec{A} + \frac{1}{c^2} \frac{\partial \varphi}{\partial t} \right) &= -\mu_0 \vec{j}, \end{aligned} \quad (1.9)$$

where we used the *Graßmann Identity*: $\vec{\nabla} \times (\vec{\nabla} \times \vec{A}) = \vec{\nabla}(\vec{\nabla} \cdot \vec{A}) - \Delta \vec{A}$.

The description of the fields by the aforementioned potentials φ and \vec{A} are not unique. This is called gauge freedom. The potentials can be specifically adjusted to the problem at hand. The gauge transformations look like

$$\begin{aligned} \vec{A} &\mapsto \vec{A}' = \vec{A} + \vec{\nabla} \psi \\ \varphi &\mapsto \varphi' = \varphi - \frac{\partial \psi}{\partial t}, \end{aligned} \quad (1.10)$$

where $\psi: \mathbb{R}^3 \times \mathbb{R} \mapsto \mathbb{R}$. In Appendix A we show, that ψ does indeed not change the physics.

If we choose ψ such that

$$\vec{\nabla} \vec{A} + \frac{1}{c^2} \frac{\partial \varphi}{\partial t} = 0, \quad (1.11)$$

then we call it a *Lorentz Gauge* and the potential Equations (1.9) decouple into two separate wave equations

$$\begin{aligned}\hat{\square}\varphi &= -\frac{\rho}{\epsilon_0} \\ \hat{\square}\vec{A} &= -\mu_0\vec{j}.\end{aligned}\tag{1.12}$$

1.3 Liénard-Wiechert Potentials

1.3.1 Solution of the inhomogeneous wave equation

The *Liénard-Wiechert* Potentials are the solution of equation (1.12). Following [15] we solve the general case

$$\hat{\square}\psi(\vec{r}, t) = f(\vec{r}, t),\tag{1.13}$$

where $\psi, f : \mathbb{R}^3 \times \mathbb{R} \mapsto \mathbb{R}$. f is called source function and will be specified later. (1.13) is a linear inhomogeneous partial differential equation. Those kind of equations are solved with the *Green's function* approach. If we can find the Green's function G fulfilling

$$\hat{\square}G(\vec{r} - \vec{r}', t - t') = -\delta(\vec{r} - \vec{r}')\delta(t - t'),\tag{1.14}$$

then we can calculate the solution of (1.13) via

$$\psi(\vec{r}, t) = \int \int G(\vec{r} - \vec{r}', t - t')f(\vec{r}, t)d\vec{r}' dt'.\tag{1.15}$$

To find G we use the following Fourier - Transformations

$$\begin{aligned}G(\vec{r} - \vec{r}', t - t') &= \frac{1}{4\pi^2} \int \int G(\vec{k}, \omega) \exp(i\vec{k}(\vec{r} - \vec{r}')) \exp(-i\omega(t - t')) d\omega d\vec{k}, \\ \delta(\vec{r} - \vec{r}') &= \frac{1}{4\pi^2} \int \exp(i\vec{k}(\vec{r} - \vec{r}')) d\vec{k}, \\ \delta(t - t') &= \frac{1}{4\pi^2} \int \exp(-i\omega(t - t')) d\omega.\end{aligned}\tag{1.16}$$

Plugging in (1.16) into (1.14) yields

$$\int \int \exp(i\vec{k}(\vec{r} - \vec{r}')) \exp(-i\omega(t - t')) \left[G(\vec{k}, \omega) \left(-k^2 + \frac{\omega^2}{c^2} \right) + \frac{1}{4\pi^2} \right] = 0,$$

which leaves us with

$$G(\vec{k}, \omega) = \frac{1}{4\pi^2} \frac{1}{k^2 - \frac{\omega^2}{c^2}}.$$

Using residue theorem we find the Fourier Back Transform of G to be

$$G_{ret}(\vec{r} - \vec{r}', t - t') = \frac{\delta(t' - t_{ret})}{4\pi |\vec{r} - \vec{r}'|}, \quad (1.17)$$

where

$$t_{ret} := t - \frac{|\vec{r} - \vec{r}'|}{c} \quad (1.18)$$

is the retarded time. We also call G_{ret} the *retarded Green's function* in contrast to the *advanced Green's function* G_{av} with the advanced time

$$t_{av} := t + \frac{|\vec{r} - \vec{r}'|}{c}. \quad (1.19)$$

The latter does not fulfill the causal principle of physics. We expect the reason for a change in our signal at \vec{r} at time t , due to a perturbation, to be in the past, not the future. Because $t_{ret} < t$ the retarded Green's function is the one to work with. Plugging in (1.17) into (1.15) yields

$$\psi(\vec{r}, t) = \frac{1}{4\pi} \int \frac{f(\vec{r}', t_{ret})}{|\vec{r} - \vec{r}'|} d\vec{r}', \quad (1.20)$$

which finally leads to the retarded potential equations

$$\varphi(\vec{r}, t) = \frac{1}{4\pi\epsilon_0} \int \frac{\rho(\vec{r}', t_{ret})}{|\vec{r} - \vec{r}'|} d\vec{r}', \quad (1.21)$$

$$\vec{A}(\vec{r}, t) = \frac{\mu_0}{4\pi} \int \frac{\vec{j}(\vec{r}', t_{ret})}{|\vec{r} - \vec{r}'|} d\vec{r}'. \quad (1.22)$$

Lastly, we show in Appendix B that they indeed fulfill the Laurentz Gauge (1.11).

1.3.2 Special Case: Moving point charge

Now we want to discuss the special case of a particle with charge q , moving along the trajectory \vec{r}_p with velocity $\vec{v} := \dot{\vec{r}}_p$, where the dot donates the time derivative. As

mentioned before, we now define the source functions for our problem at hand. For the charge density we have

$$\rho(\vec{r}, t) = q\delta(\vec{r} - \vec{r}_p(t)) \quad (1.23)$$

and for the current density

$$\vec{j}(\vec{r}, t) = q\vec{v}\delta(\vec{r} - \vec{r}_p(t)). \quad (1.24)$$

Identifying

$$\begin{aligned} \psi(\vec{r}, t) &= \varphi(\vec{r}, t) \text{ and } f(\vec{r}', t') = \frac{\rho(\vec{r}', t')}{\epsilon_0}, \\ \vec{\psi}(\vec{r}, t) &= \vec{A}(\vec{r}, t) \text{ and } \vec{f}(\vec{r}', t') = \mu_0 \vec{j}(\vec{r}', t') \end{aligned}$$

and using (1.15) with (1.17) yields after integrating over \vec{r}'

$$\begin{aligned} \varphi(\vec{r}, t) &= \frac{1}{4\pi\epsilon_0} \int \frac{\delta\left(\frac{|\vec{r}-\vec{r}_p|}{c} - t + t'\right)}{|\vec{r} - \vec{r}_p|} dt', \\ \vec{A}(\vec{r}, t) &= \frac{q\mu_0}{4\pi} \int \vec{v}(t') \frac{\delta\left(\frac{|\vec{r}-\vec{r}_p|}{c} - t + t'\right)}{|\vec{r} - \vec{r}_p|} dt'. \end{aligned} \quad (1.25)$$

For the t' - integration we need the following property of the δ - distribution

$$\delta[g(t')] = \sum_{i=1}^n \frac{\delta(t' - t_i)}{\left| \left(\frac{dg}{dt'} \right) \Big|_{t'=t_i} \right|}, \quad (1.26)$$

where

$$g(t') := \frac{|\vec{r} - \vec{r}_p|}{c} - t + t' \quad (1.27)$$

and t_i are the roots of g . To find the roots of g , let's consider

$$\begin{aligned} \frac{dg}{dt'} &= 1 + \frac{1}{c} \frac{d}{dt'} |\vec{r} - \vec{r}_p| = 1 - \frac{\vec{v}(t')}{c} \underbrace{\frac{\vec{r} - \vec{r}_p}{|\vec{r} - \vec{r}_p|}}_{|\cdot|=1} \\ &\implies 1 - \frac{\vec{v}(t')}{c} \leq \frac{dg}{dt'} \leq 1 + \frac{\vec{v}(t')}{c} \\ &\stackrel{v < c}{\implies} \frac{dg}{dt'} > 0, \end{aligned} \quad (1.28)$$

which means that g is a monotonically increasing function and therefore has at most one root, which is $t' = t_{ret}$ as can be seen from (1.27). In case that g has no roots at all, we can conclude that $\varphi \equiv 0$ and $\vec{A} \equiv 0$.

With $t_{ret} := t - \frac{|\vec{r} - \vec{r}_p|}{c}$ the integration over t' yields

$$\begin{aligned}\varphi(\vec{r}, t) &= \frac{1}{4\pi\epsilon_0} \frac{q}{|\vec{r} - \vec{r}_p(t_{ret})| - \frac{\vec{v}(t_{ret})}{c}(\vec{r} - \vec{r}_p(t_{ret}))}, \\ \vec{A}(\vec{r}, t) &= \frac{1}{4\pi} \frac{q\vec{v}(t_{ret})}{|\vec{r} - \vec{r}_p(t_{ret})| - \frac{\vec{v}(t_{ret})}{c}(\vec{r} - \vec{r}_p(t_{ret}))}\end{aligned}\quad (1.29)$$

which are the *Liénard-Wiechert Potentials*. Upon defining

$$\begin{aligned}\vec{\beta}(t) &:= \frac{\vec{v}(t)}{c}, \\ \vec{R}(\vec{r}, t) &:= \vec{r} - \vec{r}_p(t), \\ \vec{n}(\vec{r}, t) &:= \frac{\vec{R}(\vec{r}, t)}{R(\vec{r}, t)}\end{aligned}\quad (1.30)$$

we can rewrite the Liénard-Wiechert Potentials in a more compact and final form

$$\begin{aligned}\varphi(\vec{r}, t) &= \frac{1}{4\pi\epsilon_0} \frac{q}{(1 - \vec{\beta}(t') \cdot \vec{n}(\vec{r}, t')) R(\vec{r}, t')} \Big|_{t'=t_{ret}}, \\ \vec{A}(\vec{r}, t) &= \frac{\mu_0}{4\pi} \frac{q\vec{\beta}(t')}{(1 - \vec{\beta}(t') \cdot \vec{n}(\vec{r}, t')) R(\vec{r}, t')} \Big|_{t'=t_{ret}}.\end{aligned}\quad (1.31)$$

The latter potentials are the generalization of the Coulomb Potential. With the help of (1.8) the electric and magnetic fields can be derived from the *Liénard-Wiechert Potentials* (1.31). Since this is a quite longish calculation it is referred to [15] and just present the final result

$$\begin{aligned}\vec{E}(\vec{r}, t) &= \frac{q}{4\pi\epsilon_0} \left(\frac{\vec{n}(\vec{r}, t') - \vec{\beta}(t)}{\gamma^2 (1 - \vec{\beta}(t) \cdot \vec{n}(\vec{r}, t'))^3 R^2(\vec{r}, t')} \right. \\ &\quad \left. + \frac{1}{c} \frac{\vec{n}(\vec{r}, t') \times (\vec{n}(\vec{r}, t') - \vec{\beta}(t)) \times \dot{\vec{\beta}}(t)}{(1 - \vec{\beta}(t) \cdot \vec{n}(\vec{r}, t'))^3 R(\vec{r}, t')} \right) \Big|_{t'=t_{ret}}, \\ \vec{B}(\vec{r}, t) &= \frac{1}{c} \left(\vec{n}(\vec{r}, t') \times \vec{E}(\vec{r}, t) \right) \Big|_{t'=t_{ret}}.\end{aligned}\quad (1.32)$$

This is the electric and magnetic field of a moving charged particle. Due to the finite speed of light, the fields need time to travel from their source to the observation point. That means, that the fields at time t , were actually produced at an earlier time t_{ret} . As can be seen in Figure 3.1, the retarded time is determined by the intersection point of the particle trajectory with the backward lightcone of the observation point.

1.3.3 Energy emission

Now we want to discuss the energy flow and emission. Therefore, we need to analyze the Poynting Vector

$$\vec{S} = \frac{1}{\mu_0} \vec{E} \times \vec{B} = \frac{1}{\mu_0 c} \left[\vec{n}_{ret} E^2 - (\vec{n}_{ret} \vec{E}) \vec{E} \right], \quad (1.33)$$

where $\vec{n}_{ret} := \vec{n}(\vec{r}, t_{ret})$. Taking a closer look at (1.32) reveals that both \vec{E} and \vec{B} can be separated into two parts, one of which is not dependent on the particle acceleration

$$\begin{aligned} \vec{E}_{(v)}(\vec{r}, t) &= \frac{q}{4\pi\epsilon_0} \frac{1}{\gamma^2 (1 - \vec{\beta}(t') \cdot \vec{n}(\vec{r}, t'))^3 R^2(\vec{r}, t')} \left(\vec{n}(\vec{r}, t') - \vec{\beta}(t') \right) \Big|_{t' = t_{ret}} \\ \vec{B}_{(v)}(\vec{r}, t) &= \frac{q}{4\pi\epsilon_0 c} \frac{1}{\gamma^2 (1 - \vec{\beta}(t') \cdot \vec{n}(\vec{r}, t'))^3 R^2(\vec{r}, t')} \underbrace{\left[\vec{n} \times \left(\vec{n}(\vec{r}, t') - \vec{\beta}(t') \right) \right]}_{= \frac{1}{c} (\vec{v} \times \vec{n})} \Big|_{t' = t_{ret}} \end{aligned} \quad (1.34)$$

whilst the other is through $\dot{\vec{\beta}}$

$$\begin{aligned} \vec{E}_{(a)}(\vec{r}, t) &= \frac{q}{4\pi\epsilon_0 c} \frac{\vec{n}(\vec{r}, t') \times \left(\vec{n}(\vec{r}, t') - \vec{\beta}(t') \right) \times \dot{\vec{\beta}}(t')}{\left(1 - \vec{\beta}(t') \cdot \vec{n}(\vec{r}, t') \right)^3 R(\vec{r}, t')} \Big|_{t' = t_{ret}} \\ \vec{B}_{(a)}(\vec{r}, t) &= \frac{q}{4\pi\epsilon_0 c^2} \frac{\vec{n}(\vec{r}, t') \times \left[\vec{n}(\vec{r}, t') \times \left(\vec{n}(\vec{r}, t') - \vec{\beta}(t') \right) \times \dot{\vec{\beta}}(t') \right]}{\left(1 - \vec{\beta}(t') \cdot \vec{n}(\vec{r}, t') \right)^3 R(\vec{r}, t')} \Big|_{t' = t_{ret}}. \end{aligned} \quad (1.35)$$

Since $E_{(v)} \propto \frac{1}{R^2}$ whereas $E_{(a)} \propto \frac{1}{R}$, its field contributions will dominate in the far field, i.e. for large distances from the source. Plugging in (1.32) in (1.33) gives us several terms

with different orders of $\frac{1}{R}$, namely

$$\begin{aligned}\vec{S}_{vv} &\propto \left| \vec{E}_{(v)} \times \vec{B}_{(v)} \right| \propto \frac{1}{R^4}, \\ \vec{S}_{va} &\propto \left| \vec{E}_{(v)} \times \vec{B}_{(a)} \right| \propto \frac{1}{R^3}, \\ \vec{S}_{aa} &\propto \left| \vec{E}_{(a)} \times \vec{B}_{(a)} \right| \propto \frac{1}{R^2}.\end{aligned}$$

By evaluating the energy flux through an arbitrary surface with differential surface area $d\vec{\sigma}$, as illustrated in Figure 1.1.,

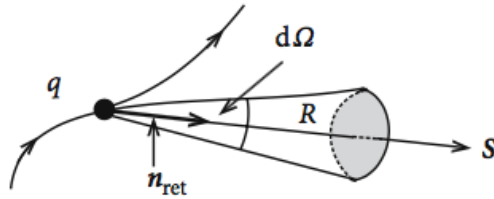


Figure 1.1.: Illustration of how to calculate the energy emission of a moving particle with charge q . [15]

we can see, that it will suffice to only consider the $\frac{1}{R^2}$ terms, because the $\frac{1}{R^3}$ or higher terms do not contribute to the energy emission, since

$$\oint \vec{S} d\vec{\sigma} \rightsquigarrow \oint \frac{1}{R^3} r^2 d\Omega \rightsquigarrow \oint \frac{1}{r} d\Omega \rightsquigarrow \frac{1}{r} \xrightarrow{r \rightarrow \infty} 0, \quad (1.36)$$

where $d\Omega := \sin(\vartheta) d\vartheta d\varphi$. That means we can focus on (1.35) when calculating (1.33)

$$\vec{S} = \frac{1}{\mu_0 c} \frac{q^2}{16\pi^2 \epsilon_0^2 c^2} \frac{\vec{n}(\vec{r}, t') \left[\vec{n}(\vec{r}, t') \times (\vec{n}(\vec{r}, t') - \vec{\beta}(t')) \times \dot{\vec{\beta}}(t') \right]^2}{\left(1 - \vec{\beta}(t') \cdot \vec{n}(\vec{r}, t') \right)^6 R^2(\vec{r}, t')} \Bigg|_{t' = t_{ret}} + \mathcal{O}\left(\frac{1}{R^3}\right) \quad (1.37)$$

The energy flux has the direction of \vec{n}_{ret} , i.e. it flows from the particle position \vec{r}_p at time $t' = t_{ret}$ to the observation point \vec{r} . We can also see, that only accelerated particles ($\dot{\vec{\beta}} \neq 0$) loose energy through radiation, which leads to a reduction in kinetic energy. Although an uniformly moving particle produces E and B - fields, it does not loose energy

through radiation.

Lastly, we want to discuss the radiation power. The emitted energy per time dt into the solid angle $d\Omega$ is described by

$$\frac{dW}{d\Omega} = \left(\vec{S} \cdot \vec{n}(\vec{r}, t') \right) R^2(\vec{r}, t') \Big|_{t'=t_{ret}}. \quad (1.38)$$

Usually the observed amount of energy per unit time dt is not the same as the emitted energy of the particle per unit time dt_{ret} . To learn more about the emission within the particles system, we want to express our equation in terms of dt_{ret} , which gives us

$$\frac{dW}{d\Omega} = \left(\vec{S} \cdot \vec{n}(\vec{r}, t') \right) R^2(\vec{r}, t') \left(\frac{dt}{dt'} \right) \Big|_{t'=t_{ret}}. \quad (1.39)$$

From the definition of $t_{ret} := t' - \frac{|\vec{r} - \vec{r}'|}{c}$ we find

$$\left(\frac{dt}{dt'} \right) \Big|_{t'=t_{ret}} = \left(1 + \frac{1}{c} \frac{d}{dt'} |\vec{r} - \vec{r}_p(t')| \right) \Big|_{t'=t_{ret}} = \left(1 - \frac{1}{c} \vec{n}(\vec{r}, t') \vec{v}(t') \right) \Big|_{t'=t_{ret}}. \quad (1.40)$$

Finally, we obtain

$$\frac{dW}{d\Omega} = \frac{q^2}{16\pi^2\epsilon_0 c} \frac{\left[\vec{n}(\vec{r}, t') \times (\vec{n}(\vec{r}, t') - \vec{\beta}(t')) \times \dot{\vec{\beta}}(t') \right]^2}{\left(1 - \vec{\beta}(t') \cdot \vec{n}(\vec{r}, t') \right)^5} \Big|_{t'=t_{ret}}. \quad (1.41)$$

Now we can discuss two cases. The non relativistic case ($\beta \approx 0$) and the relativistic case ($\beta \approx 1$).

$\beta \approx 0$: In this case (1.41) simplifies to

$$\begin{aligned} \frac{dW}{d\Omega} &= \frac{q^2}{16\pi^2\epsilon_0 c} \left[\vec{n}(\vec{r}, t') \times (\vec{n}(\vec{r}, t') \times \dot{\vec{\beta}}(t')) \right]^2 \Big|_{t'=t_{ret}} \\ &= \frac{q^2}{16\pi^2\epsilon_0 c} \left[\underbrace{(\vec{n}(\vec{r}, t') \cdot \dot{\vec{\beta}}(t'))}_{=\dot{\beta}n \cos(\vartheta)} \vec{n}(\vec{r}, t') - \underbrace{(\vec{n}(\vec{r}, t') \cdot \vec{n}(\vec{r}, t'))}_{|\cdot|=1} \dot{\vec{\beta}}(t') \right]^2 \Big|_{t'=t_{ret}} \\ &= \frac{q^2 \dot{\beta}_{ret}^2}{16\pi^2\epsilon_0 c} (\cos^2(\vartheta) - 2 \cos^2(\vartheta) + 1) \\ &= \frac{q^2 \dot{\beta}_{ret}^2}{16\pi^2\epsilon_0 c} \sin^2(\vartheta), \end{aligned}$$

where ϑ is the angle between $\dot{\vec{\beta}}$ and \vec{n} . β_{ret} means again the evaluation at $t' = t_{ret}$. We conclude that the direction of maximum radiation is perpendicular to the particles direction of motion, in contrast to

$\beta \approx 1$: where we will see shortly that the maximum radiation will be primarily in the direction of motion of the particle. We will restrict ourselves to the simple case, where $\dot{\vec{\beta}} \parallel \vec{\beta}$. Following the same steps as above we obtain

$$\frac{dW}{d\Omega} = \frac{q^2 \dot{\beta}_{ret}^2}{16\pi^2 \epsilon_0 c} \frac{\sin^2(\vartheta)}{(1 - \beta(t') \cos(\vartheta))^5}. \quad (1.42)$$

To get the angle, where the radiation is maximal, we calculate

$$\begin{aligned} \frac{d}{d(\cos(\vartheta))} \left(\frac{dW}{d\Omega} \right) &\stackrel{!}{=} 0 \\ \iff -2 \cos(\vartheta) (1 - \beta_{ret} \cos(\vartheta))^5 + 5\beta_{ret}(1 - \cos^2(\vartheta))(1 - \beta_{ret} \cos(\vartheta))^4 &\stackrel{!}{=} 0 \\ \iff (1 - \beta_{ret} \cos(\vartheta))^4 [-2 \cos(\vartheta) (1 - \beta_{ret} \cos(\vartheta)) + 5\beta_{ret}(1 - \cos^2(\vartheta))] &\stackrel{!}{=} 0 \\ \iff -2 \cos(\vartheta) (1 - \beta_{ret} \cos(\vartheta)) + 5\beta_{ret}(1 - \cos^2(\vartheta)) &\stackrel{!}{=} 0 \\ \iff \cos^2(\vartheta) + \frac{2}{3\beta_{ret}} \cos(\vartheta) - \frac{5}{3} &\stackrel{!}{=} 0 \\ \implies \cos(\vartheta)_{max} &= \frac{1}{3\beta_{ret}} \left(\sqrt{1 + 15\beta_{ret}^2} - 1 \right). \end{aligned}$$

Obviously the angle decreases monotonically with increasing velocity, i.e. increasing β_{ret} . For $\beta_{ret} = 1$ we get $\cos(\vartheta) = 1$ or equivalently $\vartheta = 0$. In Figure 1.2 the results are summarized.

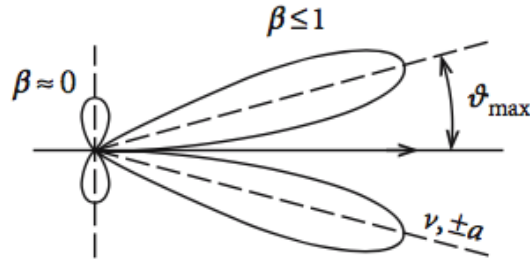


Figure 1.2.: Radiation characteristics of a moving charged particle. [15]

Part II.

Numerics

The following section deals with the numeric aspects of this thesis. We explain the underlying equation of motions and their history. After that, we go into several methods with which we can solve differential equations. Over the course of the last decades numerous methods were invented each of which has its own strengths and weaknesses. Some of them are very easy to implement, which in turn usually leads to unprecise results. Others are quite complicated and sophisticated to implement, but very accurate. Therefore, one should always consider which method is best for the problem and what it is one want to achieve.

Following this, we also want to define and calculate the numerical complexity of some chosen algorithms.

2

Integration of Equation of Motion

2.1 Equations of Motion

As we know from mechanics the dynamics of particles is determined by the forces acting on them. In our case there is a force due to electro-magnetic fields. That can be external fields, but also fields due to moving particles, as we explained in Section 1.3.

The dynamics of our system is described by the *Lorentz-Newton* equations

$$\begin{aligned} \frac{dx^\mu}{d\tau} &= u^\mu \\ \frac{du^\mu}{d\tau} &= F_\nu^\mu u^\nu + g^\mu. \end{aligned} \quad (2.1)$$

The term F_ν^μ describes the electromagnetic field strength tensor

$$F_\nu^\mu = \begin{pmatrix} 0 & E_x & E_y & E_z \\ E_x & 0 & B_z & -B_y \\ E_y & -B_z & 0 & B_x \\ E_z & B_y & -B_x & 0 \end{pmatrix}. \quad (2.2)$$

The damping term g^μ considers the fact that charged particles radiate fields when they are moving which leads to a loss in their kinetic energy. Within the context of classical electrodynamics Max *Abraham* and Hendrick *Lorentz* discussed radiation damping in their same-named equation first. In 1938 *Dirac* generalized the equation whilst taking special relativity into account [10]. It turned out, however, that this equation has unphysical solutions, which violate the causality principle. *Landau* and *Lifschitz* solved this problem using perturbation theory [14]. The Landau-Lifschitz equation reads

$$\begin{aligned} g^\mu = \frac{\mu_0 q^2}{6\pi c} \left(\frac{q}{m_e} \frac{\partial F^{\mu\nu}}{\partial x^\xi} u^\nu u^\xi - \frac{e^2}{m_e^2} F^{\mu\xi} F_{\nu\xi} u^\nu \right. \\ \left. + \frac{q^2}{m_e^2 c^2} (F_{\nu\xi} u^\xi) (F^{\nu\pi} u_\pi) u^\mu \right). \quad (2.3) \end{aligned}$$

In this thesis the damping term g^μ is neglected. In [1] a rough estimation shows that radiation damping of an electron gyrating in a constant B field with frequency ω_0 can be neglected if

$$\omega_0 \Delta \tilde{t} \ll 1 \quad (2.4)$$

holds. $\Delta \tilde{t} = \frac{q^2}{4\pi\epsilon_0 m_e c^3} = 9.40 \cdot 10^{-24}$ s is the normalized time. In Section 4.8 we show, that equation (2.4) is indeed fulfilled in our simulations.

We now want to present different methods of how to solve the Lorentz-Newton equation (2.1) numerically.

2.2 Euler-Scheme

The most simple method is the explicit *Euler*-Method. It's easy to implement but not very accurate, as we shall see later. But before we go into the details of the explicit Euler-Scheme we need to address some prerequisites all following methods will have in common.

Starting point will always be a first order system of the kind

$$\begin{aligned} \frac{dx^\mu}{d\tau} &= u^\mu \\ \frac{du^\mu}{d\tau} &= f^\mu(x^\nu, u^\nu) \\ x^\mu(\tau_0) &= x_0^\mu \\ u^\mu(\tau_0) &= u_0^\mu. \end{aligned} \quad (2.5)$$

Systems of higher order can always be reduced to a first order system.

In order to solve the equation of motion numerically the domain needs to be discretized. Therefore, we divide the time interval into N equidistant partial intervals h , by defining

$$h := \Delta\tau = \tau_{i+1} - \tau_i.$$

The idea is to calculate each point along the trajectory $x_i^\mu = x^\mu(\tau_i)$ iteratively, starting from the initial values x_0^μ and u_0^μ . But to calculate these points all differential operators in (2.5) need to be discretized as well. That is where all methods differ. Each method has its own way to discretize the differential operators.

The basis of the Euler-Scheme is a first order Taylor expansion of the integration variable x^μ in τ around τ_i

$$x^\mu(\tau_{i+1}) = x^\mu(\tau_i) + \left. \frac{dx^\mu}{d\tau} \right|_{\tau=\tau_i} \underbrace{(\tau_{i+1} - \tau_i)}_{=h} + \mathcal{O}(h^2). \quad (2.6)$$

Analogously for u^μ and solving for $\frac{dx^\mu}{d\tau}$ and $\frac{du^\mu}{d\tau}$ respectively yields

$$\begin{aligned}\frac{x_{i+1}^\mu - x_i^\mu}{h} &= u_i^\mu \\ \frac{u_{i+1}^\mu - u_i^\mu}{h} &= f^\mu(x_i^\nu, u_i^\nu).\end{aligned}\tag{2.7}$$

This way of discretizing allows a very easy calculation of x_i^μ according to

$$\begin{aligned}x_{i+1}^\mu &= x_i^\mu + h u_i^\mu \\ u_{i+1}^\mu &= u_i^\mu + h f^\mu(x_i^\nu, u_i^\nu).\end{aligned}\tag{2.8}$$

In order for us to calculate the goodness of this approximation we need to introduce the *Procedural Error* and the *Order of Consistency* [13].

2.2.1 Procedural Error and Order of Consistency

Definition 2.2.1 (Procedural Error and Order of Consistency) Let $I \subseteq \mathbb{R}$ be a interval, $f : I \times \mathbb{R}^d \rightarrow \mathbb{R}^d$, $y : I \rightarrow \mathbb{R}^d$ a solution of the initial value problem

$$\begin{aligned}\frac{d}{d\tau}y(\tau) &= f(\tau, y(\tau)), \\ y(\tau_0) &= y_0.\end{aligned}\tag{2.9}$$

(a) The term

$$\eta(\tau, h) := y(\tau) + h f(\tau, y(\tau)) - y(\tau + h) \quad \text{for } \tau \in I, 0 < h \leq b - \tau \tag{2.10}$$

is called local Procedural Error of the One-Step-Scheme at τ for the increment h .

(b) The One-Step-Scheme has an Order of Consistency $p \geq 1$, if the local Procedural Error fulfils

$$\|\eta(\tau, h)\| \leq Ch^{p+1} \quad \text{for } \tau \in I, 0 < h \leq b - \tau, \tag{2.11}$$

with a constant $C \geq 0$, which is independent of τ and h .

Descriptively the Procedural Error is the difference between the exact solution $y(\tau + h)$ and the result, which we get from the One-Step-Scheme starting from the exact solution at the earlier time step $y(\tau)$. Figure 2.1 illustrates the situation.

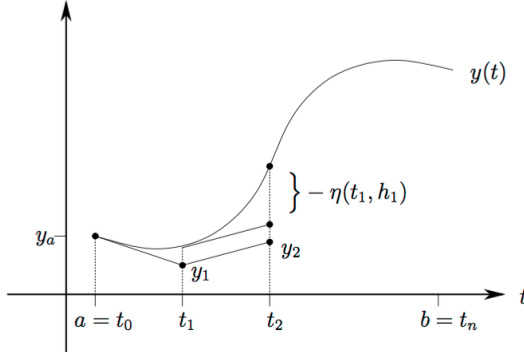


Figure 2.1.: Illustration of the Procedural Errors of an One-Step-Scheme. [13]

We now want to use the definitions 2.2.1 to calculate the Order of Consistency of the Euler-Scheme.

Starting point is the system (2.1). Thereby we focus on the equation for u^μ , since x^μ can be easily integrated from u^μ . Following Definition 2.2.1 we have

$$y = u^\mu. \quad (2.12)$$

We get

$$\eta(\tau, h) = u^\mu(\tau_i) + h f^\mu(x^\nu, u^\nu) - u^\mu(\tau_{i+1}). \quad (2.13)$$

The last term can be calculated with a Taylor-expansion analogously to (2.6).

$$u^\mu(\tau_{i+1}) = u^\mu(\tau_i) + h \frac{du^\mu}{d\tau} \Big|_{s=\tau_i} + h^2 \frac{d^2 u^\mu}{d\tau^2} \Big|_{s=\tau_i}. \quad (2.14)$$

Plugging in (2.14) in (2.13) yields

$$\begin{aligned} \eta(\tau, h) &= u^\mu(\tau_i) + h \frac{du^\mu}{d\tau} - u^\mu(\tau_{i+1}) \\ \stackrel{(2.14)}{\implies} \eta(\tau, h) &= u^\mu(\tau_i) + h \frac{du^\mu}{d\tau} - u^\mu(\tau_i) - h \frac{du^\mu}{d\tau} - h^2 \frac{d^2 u^\mu}{d\tau^2} \\ \iff \eta(\tau, h) &= \frac{d^2 u^\mu}{d\tau^2} h^2, \end{aligned} \quad (2.15)$$

since $\frac{du^\mu}{d\tau} = f^\mu(x^\nu, u^\nu)$ holds for the Euler-Scheme. Thus

$$|\eta(\tau, h)| \leq Ch^2 \quad \text{with } C := \frac{1}{2} \max_{\tau \in \mathcal{D}(u^\mu)} \left| \frac{d^2 u^\mu}{d\tau^2} \right|. \quad (2.16)$$

$\mathcal{D}(u^\mu)$ denotes the domain of u^μ . Therefore, the Euler-Scheme has an Order of Consistency of one.

2.3 Leap-Frog-Scheme

A definitely better method is the so called *Leap-Frog-Scheme*. One can easily proof that it has an Order of Consistency of two.

In contrast to the explicit Euler-Scheme this method has several advantages. For one, it is time reversible, i.e. it is possible to reach any previous point in time from every point later in the trajectory. On the other hand, the Leap-Frog-Scheme is symplectic, meaning it conserves the phase space volume from which energy and momentum conservation follows.

However, one disadvantage is that it's only suited for systems in which the acting force exclusively depends on the current position, but not on the velocity of the particle. This would lead to an implicit equation system which is numerically way more expensive to solve.

Thus the differential equation should be of the form

$$\frac{d^2 x^\mu}{d\tau^2} = \frac{du^\mu}{d\tau} = f^\mu(x^\nu). \quad (2.17)$$

As we already mentioned, the various methods discretize the differential operators differently. The Leap-Frog-Scheme uses

$$\begin{aligned} \frac{x_{i+1}^\mu - x_i^\mu}{h} &= u_{i+\frac{1}{2}}^\mu \\ \frac{u_{i+\frac{1}{2}}^\mu - u_{i-\frac{1}{2}}^\mu}{h} &= f^\mu(x_i^\nu). \end{aligned} \quad (2.18)$$

Solving for the new time step yields

$$\begin{aligned} x_{i+1}^\mu &= x_i^\mu + hu_{i+\frac{1}{2}}^\mu \\ u_{i+\frac{1}{2}}^\mu &= u_{i-\frac{1}{2}}^\mu + hf^\mu(x_i^\nu). \end{aligned} \quad (2.19)$$

As we can see, position and velocity are calculated at different times. They are shifted against each other in time by $h = \frac{1}{2}$.

But what if we have a system in which the force depends on the velocity? Are we stuck with expensive implicit methods? Fortunately not. We can use the *Boris* - Method.

2.3.1 Boris-Method

This method was invented in 1970 by J.P. Boris [5] and is the standard method for pushing particles in plasma simulations today. We want to solve the Lorentz-Newton equation

$$\frac{v_{i+\frac{1}{2}} - v_{i-\frac{1}{2}}}{h} = \frac{q}{m} \left(\vec{E} + \frac{v_{i+\frac{1}{2}} + v_{i-\frac{1}{2}}}{2} \times \vec{B} \right) \quad (2.20)$$

Boris noticed, that upon defining

$$\begin{aligned} \vec{v}_- &:= v_{i-\frac{1}{2}} + \frac{h}{2} \frac{q\vec{E}}{m} \quad \text{and} \\ \vec{v}_+ &:= v_{i+\frac{1}{2}} + \frac{h}{2} \frac{q\vec{E}}{m}, \end{aligned} \quad (2.21)$$

one can eliminate the electric field. Plugging in (2.21) into (2.20) yields

$$\begin{aligned} \frac{\vec{v}_+ - \vec{v}_-}{h} &= \frac{q}{m} (\vec{v}_+ + \vec{v}_-) \times \vec{B} \\ \implies |\vec{v}_+ - \vec{v}_-| &= \frac{qh}{m} |\vec{v}_+ + \vec{v}_-| B \underbrace{\sin(\vartheta)}_{=1}, \end{aligned} \quad (2.22)$$

where ϑ is the angle between \vec{B} and \vec{v} . By splitting up the accelerating effect of the electric field in two parts with the rotational effect of the magnetic field in between, the accuracy is increased without having computational overhead. Hence, the steps are

1. Obtain \vec{v}_- by starting from $v_{i-\frac{1}{2}}$ and adding half electric impulse.
2. Use rotation in (2.22) to obtain \vec{v}_+ and finally
3. obtain $v_{i+\frac{1}{2}}$ by adding yet another half electric impulse.

In the code used in this master thesis, the slightly more sophisticated but relativistically correct form with $u = \gamma v$ is used.

Up to now one question remains unanswered. How do we solve for \vec{v}_+ in (2.22)? To answer this, we use Figure 2.2.

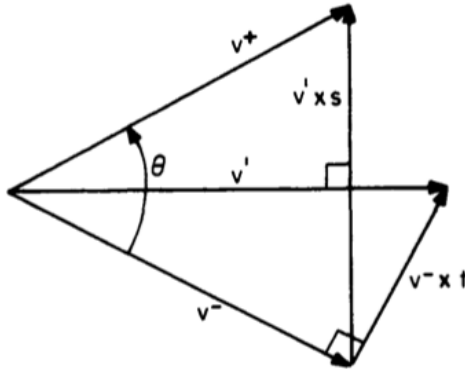


Figure 2.2.: Velocity space showing the rotation from \vec{v}_- to \vec{v}' . The velocities shown are projections of the total velocities onto the plane perpendicular to \vec{B} . [6]

What we want is a vector, which is parallel to $\vec{v}_+ - \vec{v}_-$. Its magnitude is yet to be determined. However, if we can find a vector \vec{v}' which is perpendicular to $\vec{v}_+ - \vec{v}_-$, then $\vec{v}' \times \vec{s}$, where $\vec{s} \propto \vec{B}$, is exactly what we need.

Upon defining

$$\vec{t} := -\frac{\vec{B}}{B} \tan\left(\frac{\theta}{2}\right) = \frac{q\vec{B}h}{2m}, \quad (2.23)$$

we obtain \vec{v}' from

$$\vec{v}' = \vec{v}_- + \vec{v}_- \times \vec{t}. \quad (2.24)$$

Now \vec{v}' is perpendicular to $\vec{v}_+ - \vec{v}_-$. Finally, we need a vector $\vec{s} \propto \vec{B}$ which magnitude is determined by the constraint $|\vec{v}_+| = |\vec{v}_-|$. Using half angle formulas we find

$$\vec{s} = \frac{2\vec{t}}{1+t^2}. \quad (2.25)$$

Hence,

$$\vec{v}_+ = \vec{v}_- + \vec{v}' \times \vec{s}. \quad (2.26)$$

Finally, we want to do a quick error analysis. We expect the angle of rotation θ to be close to

$$\omega_c h = \frac{2\pi h}{T} = \frac{qBh}{m},$$

where T is the period.

Following the geometrical analysis in [6] illustrated in 2.3 and using (2.22) we find

$$\begin{aligned} \left| \tan\left(\frac{\theta}{2}\right) \right| &= \frac{\frac{1}{2}|\vec{v}_+ - \vec{v}_-|}{\frac{1}{2}|\vec{v}_+ + \vec{v}_-|} = \frac{qB}{m} \frac{h}{2} = \frac{\omega_c h}{2} \\ \implies \theta &= 2 \arctan\left(\frac{\omega_c h}{2}\right) = \omega_c h \left(1 - \frac{\omega_c^2 h^2}{12} + \dots\right). \end{aligned} \quad (2.27)$$

For $\omega_c h < 0.35$ we get an error smaller than 1%.

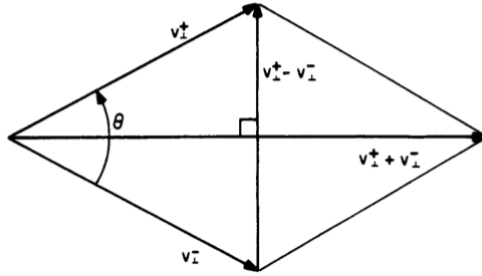


Figure 2.3.: Determination of $|\tan\left(\frac{\theta}{2}\right)|$ from boris rotation [6]

3

Interpolations

3.1 Linear interpolation of Trajectories

The previously presented methods calculate the particle trajectory solely at discrete points in time $x_i^\mu(\tau)$. Calculating Liénard-Wiechert fields according to equation (1.32), however, requires the intersection point of the trajectory with the backward lightcone of the observation point. In most cases the calculated points of the trajectory are not lying directly on the lightcone, so we need a procedure to calculate the intersection point exactly.

The simplest solution is a linear interpolation between the last point inside and the first point outside the lightcone. Figure 3.1 illustrates the situation. Thereto let $x_j^\mu \in \mathbb{R}^{3+1}$ be the last point inside and $x_{j+1}^\mu \in \mathbb{R}^{3+1}$ the first point outside the lightcone. Further let $x_c^\mu \in \mathbb{R}^{3+1}$ be the intersection point of interest then we get

$$x_c^\mu = x_j^\mu + \lambda \left(x_{j+1}^\mu - x_j^\mu \right), \quad (3.1)$$

where $\lambda \in [0, 1]$. Due to the finite speed of light the intersection point x_c^μ needs to fulfill

$$|\vec{x}_o(t) - \vec{x}_c(t_{ret})| = c (t - t_{ret}) \iff (x_o - x_c)_\mu (x_o - x_c)^\mu = 0. \quad (3.2)$$

Thereby $x_o^\mu \in \mathbb{R}^{3+1}$ denotes the observation point where the fields shall be calculated. Note, that on the left hand side of (3.2) only spatial components of the respective four vectors are used.

Plugging in (3.1) in (3.2) yields

$$\begin{aligned} & \lambda^2 (x_{j+1} - x_j)_\mu (x_{j+1} - x_j)^\mu + \lambda 2(x_{j+1} - x_j)_\mu (x_j - x_o)^\mu + (x_j)_\mu (x_j)^\mu \\ & + (x_o)_\mu (x_o)^\mu - 2(x_j)_\mu (x_o)^\mu = 0. \end{aligned} \quad (3.3)$$

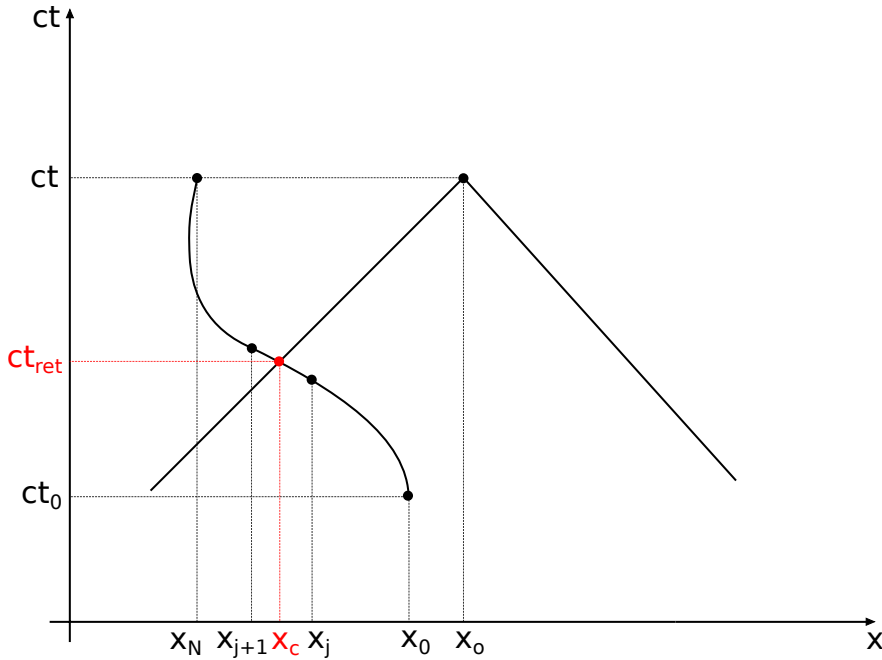


Figure 3.1.: Minkowski space showing the particle trajectory with starting point $x_0^\mu(t_0)$ and last point $x_N^\mu(t)$. The observation point $x_o^\mu(t)$ with its backward lightcone is also shown. If we want to calculate the Liénard-Wiechert fields at the observation point $x_o^\mu(t)$, we need the intersection point $x_c^\mu(t_{ret})$ of the trajectory with the backward lightcone.

We define

$$\begin{aligned} a &:= (x_{j+1} - x_j)_\mu (x_{j+1} - x_j)^\mu \\ b &:= 2(x_{j+1} - x_j)_\mu (x_j - x_o)^\mu \\ c &:= (x_j)_\mu (x_j)^\mu + (x_o)_\mu (x_o)^\mu - 2(x_j)_\mu (x_o)^\mu. \end{aligned}$$

In general the quadratic equation (3.3) in λ has two solutions

$$\lambda_{1/2} = \frac{-b \pm \sqrt{b^2 - 4ac}}{2a}.$$

One solution denotes the intersection point with the backward lightcone, the other one with the forward lightcone. Since $\lambda \in [0, 1]$ we are only interested in the larger one.

$$\lambda_{1/2} = \frac{-b + \sqrt{b^2 - 4ac}}{2a}.$$

Plugging in λ in (3.1) gives the desired intersection point.

3.2 Trilinear Interpolation of Fields

Another interpolation method we are using is the trilinear interpolation to calculate the field values at the particle position more accurately. As is explained in more detail later (see Chapter 4), field values will either be stored on grid points or calculated analytically. However, if we want to consider interactions between multiple particles correctly, we need the field values at the particle position which does usually not coincide with the grid point where the field values are stored. Matters were complicated further by the fact that our grid will be staggered, due to numerical stability issues and is explained in more detail in Section 4.1.

Let's assume we have a cube with the points A, B, C, ..., H, as is illustrated in the following Figure 3.2

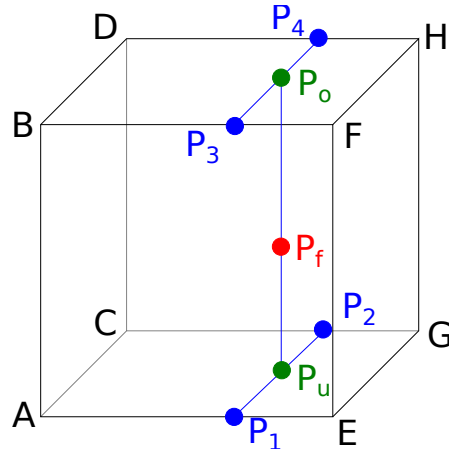


Figure 3.2.: Cube with its eight corner points A, B, C, ..., H and interpolation point P_f . The points P_1 , P_2 , P_3 and P_4 are the result of an interpolation along x direction of the lines \overline{AE} , \overline{CG} , \overline{BF} and \overline{DH} . P_u and P_o are obtained by interpolating along y - axis of the lines $\overline{P_1P_2}$ and $\overline{P_3P_4}$. Finally, P_f can be obtained by interpolating along z direction of the line $\overline{P_uP_o}$.

Those eight points are part of the grid and contain the field values for both \vec{E} and \vec{H} . To get the correct field values at the particle position $\textcolor{red}{P}_f$ we need to interpolate in 3D. The trilinear interpolation simply consists out of seven linear interpolations. We first interpolate the x -value along \overline{AE} , \overline{CG} , \overline{BF} and \overline{DH} to get the points P_1 , P_2 , P_3 and P_4 . Thereto let $x_p \in \mathbb{R}$ be the particle's x position and $x_0 \in \mathbb{R}$ and $x_1 \in \mathbb{R}$ be the corresponding x -values at A and E respectively. Same holds for the aforementioned tuples as well. Then we can write

$$\begin{aligned} u &:= \frac{x_p - x_0}{x_1 - x_0} \\ \implies P_1 &= A + u(E - A) \\ \implies P_2 &= C + u(G - C) \\ \implies P_3 &= B + u(F - B) \\ \implies P_4 &= D + u(H - D). \end{aligned} \tag{3.4}$$

In the next step, we interpolate along the y -axis. Analogously we define y_p , y_0 and y_1 . We conclude

$$\begin{aligned} v &:= \frac{y_p - y_0}{y_1 - y_0} \\ \implies P_u &= P_1 + v(P_2 - P_1) \\ \implies P_o &= P_3 + v(P_4 - P_3). \end{aligned} \tag{3.5}$$

And finally with z_p , z_0 and z_1 we get

$$\begin{aligned} w &:= \frac{z_p - z_0}{z_1 - z_0} \\ \implies P_f &= \textcolor{green}{P}_u + v(\textcolor{green}{P}_o - \textcolor{blue}{P}_u). \end{aligned} \tag{3.6}$$

4

Hybrid Field Approach

In this section we introduce the concept of hybrid fields. Christian Herzing developed this concept in his dissertation [12] and showed how this approach reduces the numerical complexity from N^2 to N . Usually the numerical complexity of multi particle simulation is N^2 , due to the interaction between each particle. In our case we need N push operations for the particles. One push for each particle. In order to do that, however, equation (2.1) needs to be solved and therefore all Liénard-Wiechert fields from the other $N - 1$ particles are needed. This results in $N(N - 1)$ calculations for each time step. If we want to calculate the Liénard-Wiechert fields, we also need to store all positions from all particles, as explained in Section 3.1. For a few particles such simulations are effortlessly feasible. But with increasing particle numbers such simulations may not just require more and more memory capacity but also become so time consuming that at some point we simply can not do them any longer. That's where the hybrid field model comes in. Instead of calculating the Liénard-Wiechert fields at every time step for all particles at all grid points, the fields are stored onto the grid and propagated through the grid using Maxwell equations. How that works in detail is explained in the following sections.

4.1 FDTD

In this section we talk about how to solve the Maxwell Equations (1.2) and how to propagate the fields on a numerical grid. We thereby focus on the Maxwell Equations in vacuum, i.e. $\rho = \vec{j} = 0$. As can be seen in the Liénard-Wiechert formula (1.32) there is a singularity for the field values at the particle position itself. Thus, we just want to propagate fields far away from the source, which is explained in more detail later.

To push the fields on the grid, i.e solving for the fields at the next time step, we use the Yee - Scheme introduced by *Kane Yee* in 1966 [22] or equivalently *Finite Difference Time Domain Method* to discretize the Maxwell Equations. Each point on the discretized grid is represented as a tuple (i, j, k) . One index for each dimension (x, y, z) . The distance between the grid points are $(\Delta x, \Delta y, \Delta z)$ respectively. h denotes the time discretization as before. In order to have finite central differences rather than plain finite

differences, the evaluation of \vec{E} and \vec{H} components are shifted in time about $\frac{h}{2}$ against each other. To have the same benefits for the rotation, the \vec{E} and \vec{H} components are shifted in space as well, as it's illustrated in Figure 4.1.

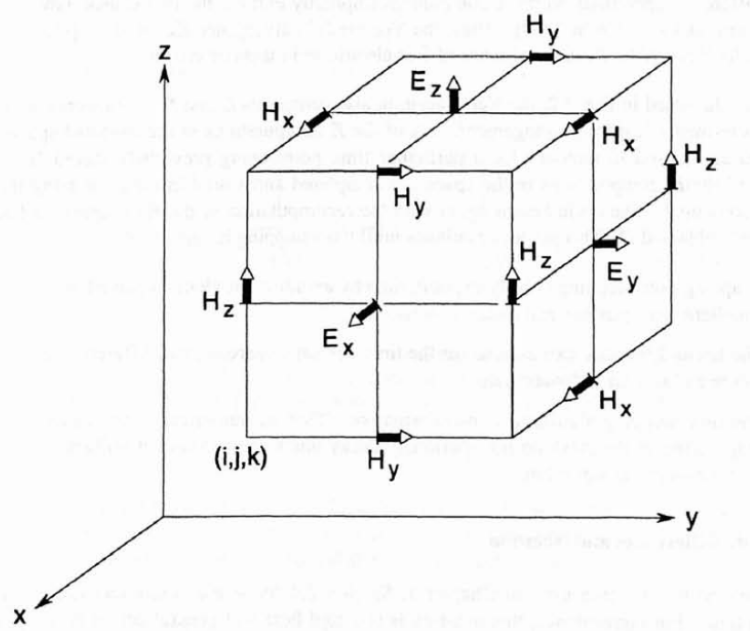


Figure 4.1.: An illustration of a so called Yee-Box which is used to solve the curl Maxwell Equations. Shown are the positions of the electric and magnetic field vector components about a cubic unit cell of the Yee space lattice. The Yee algorithm centers its E and H components in three- dimensional space so that every E component is surrounded by four circulating H components, and every H component is surrounded by four circulating E components [20].

The discrete Maxwell equations then read

$$\begin{aligned} \frac{\vec{E}|_{(i,j,k)}^{n+\frac{1}{2}} - \vec{E}|_{(i,j,k)}^{n-\frac{1}{2}}}{h} &= \vec{\nabla}^- \times \vec{H}|_{(i,j,k)}^n, \\ \frac{\vec{H}|_{(i,j,k)}^{n+1} - \vec{H}|_{(i,j,k)}^n}{h} &= \vec{\nabla}^+ \times \vec{E}|_{(i,j,k)}^{n+\frac{1}{2}}. \end{aligned} \quad (4.1)$$

The operators $\vec{\nabla}^-$ and $\vec{\nabla}^+$ act on a discretized vector field $F|_{(i,j,k)} : \mathbb{R}^3 \rightarrow \mathbb{R}$ as follows

$$\vec{\nabla}^- F|_{(i,j,k)} := \left(\frac{F|_{(i,j,k)} - F|_{(i-1,j,k)}}{\Delta x}, \frac{F|_{(i,j,k)} - F|_{(i,j-1,k)}}{\Delta y}, \frac{F|_{(i,j,k)} - F|_{(i,j,k-1)}}{\Delta z} \right)^T, \quad (4.2)$$

$$\vec{\nabla}^+ F|_{(i,j,k)} := \left(\frac{F|_{(i+1,j,k)} - F|_{(i,j,k)}}{\Delta x}, \frac{F|_{(i,j+1,k)} - F|_{(i,j,k)}}{\Delta y}, \frac{F|_{(i,j,k+1)} - F|_{(i,j,k)}}{\Delta z} \right)^T \quad (4.3)$$

where T denotes the transpose as usual. The spatial positions where \vec{E} and \vec{H} components will be calculated are given by

$$\begin{aligned} \vec{E}|_{(i,j,k)} &= \begin{pmatrix} E_x [(i + \frac{1}{2}) \Delta x, j \Delta y, k \Delta z] \\ E_y [i \Delta x, (j + \frac{1}{2}) \Delta y, k \Delta z] \\ E_z [i \Delta x, j \Delta y, (k + \frac{1}{2}) \Delta z] \end{pmatrix}, \\ \vec{H}|_{(i,j,k)} &= \begin{pmatrix} H_x [i \Delta x, (j + \frac{1}{2}) \Delta y, (k + \frac{1}{2}) \Delta z] \\ H_y [(i + \frac{1}{2}) \Delta x, j \Delta y, (k + \frac{1}{2}) \Delta z] \\ H_z [(i + \frac{1}{2}) \Delta x, (j + \frac{1}{2}) \Delta y, \Delta z] \end{pmatrix}. \end{aligned} \quad (4.4)$$

4.2 Numeric Dispersion Relation

By discretizing the numerical grid, the dispersion relation of light also changes. To study this effect we need to solve the discretized Maxwell Equations (4.1). Without loss of generality we choose the Ansatz of a TMz-mode, i.e. $H_z = 0$ and $E_z \neq 0$:

$$\begin{aligned} E_z|_{(i,j,k)}^n &= E_{z0} \exp \left\{ \hat{i} \left(\tilde{k}_x i \Delta x + \tilde{k}_y j \Delta y - \omega n h \right) \right\} \\ H_x|_{(i,j,k)}^n &= H_{x0} \exp \left\{ \hat{i} \left(\tilde{k}_x i \Delta x + \tilde{k}_y j \Delta y - \omega n h \right) \right\} \\ H_y|_{(i,j,k)}^n &= H_{y0} \exp \left\{ \hat{i} \left(\tilde{k}_x i \Delta x + \tilde{k}_y j \Delta y - \omega n h \right) \right\}, \end{aligned} \quad (4.5)$$

where \hat{i} denotes the imaginary unit and \tilde{k}_x , \tilde{k}_y the x- and y-components of the wave vector. Using TMz-mode, equation (4.1) also simplifies to

$$\begin{aligned} \frac{E_z|_{(i,j,k)}^{n+\frac{1}{2}} - E_z|_{(i,j,k)}^{n-\frac{1}{2}}}{h} &= \left(\frac{H_y|_{(i,j,k)}^n - H_y|_{(i-1,j,k)}^n}{\Delta x} - \frac{H_x|_{(i,j,k)}^n - H_x|_{(i,j-1,k)}^n}{\Delta y} \right) \\ \frac{H_x|_{(i,j,k)}^{n+1} - H_x|_{(i,j,k)}^n}{h} &= - \left(\frac{E_z|_{(i,j+1,k)}^{n+\frac{1}{2}} - E_z|_{(i,j,k)}^{n+\frac{1}{2}}}{\Delta y} \right) \\ \frac{H_y|_{(i,j,k)}^{n+1} - H_y|_{(i,j,k)}^n}{h} &= \left(\frac{E_z|_{(i+1,j,k)}^{n+\frac{1}{2}} - E_z|_{(i,j,k)}^{n+\frac{1}{2}}}{\Delta x} \right). \end{aligned} \quad (4.6)$$

Upon substituting (4.5) in (4.6) and after some manipulation we find

$$E_{z_0} \sin\left(\frac{\omega h}{2}\right) = h \left[\frac{H_{x_0}}{\Delta y} \sin\left(\frac{\tilde{k}_y \Delta y}{2}\right) - \frac{H_{y_0}}{\Delta x} \sin\left(\frac{\tilde{k}_x \Delta x}{2}\right) \right] \quad (4.7)$$

$$H_{x_0} = \frac{h E_{z_0}}{\Delta y} \frac{\sin\left(\frac{\tilde{k}_y \Delta y}{2}\right)}{\sin\left(\frac{\omega h}{2}\right)} \quad (4.8)$$

$$H_{y_0} = \frac{h E_{z_0}}{\Delta x} \frac{\sin\left(\frac{\tilde{k}_x \Delta x}{2}\right)}{\sin\left(\frac{\omega h}{2}\right)}. \quad (4.9)$$

Plugging in (4.8) and (4.9) in (4.6) we obtain the numerical dispersion relation

$$\left[\frac{1}{h} \sin\left(\frac{\omega h}{2}\right) \right]^2 = \left[\frac{1}{\Delta x} \sin\left(\frac{\tilde{k}_x \Delta x}{2}\right) \right]^2 + \left[\frac{1}{\Delta y} \sin\left(\frac{\tilde{k}_y \Delta y}{2}\right) \right]^2 \quad (4.10)$$

For the one dimensional case equation (4.10) reduces to

$$\omega h = 2 \arcsin \left(\frac{\Delta t}{\Delta x} \sin\left(\frac{\tilde{k}_x \Delta x}{2}\right) \right), \quad (4.11)$$

which is still more complicated than the analytic dispersion relation

$$\omega = k. \quad (4.12)$$

In Figure 4.2 both, the analytical and the numerical dispersion relation are plotted. Equation (4.11) has a maximum at

$$\begin{aligned} \tilde{k}_x^{max} &= \frac{\pi}{\Delta x} \\ \iff \lambda_x^{max} &= 2\Delta x. \end{aligned} \quad (4.13)$$

\tilde{k}_x^{max} is the largest possible wavevector - also called *Nyquist Limit* for a numerical grid with resolution Δx , or Δy , Δz respectively. At this wavevector, the group velocity

$$v_g = \left. \frac{\partial \tilde{k}_x}{\partial \omega} \right|_{\tilde{k}=\tilde{k}^{max}} = 0 \quad (4.14)$$

vanishes, instead of propagating with speed of light. That means, that the Yee-Scheme is only valid for wavelengths $\lambda \ll \lambda^{max}$.

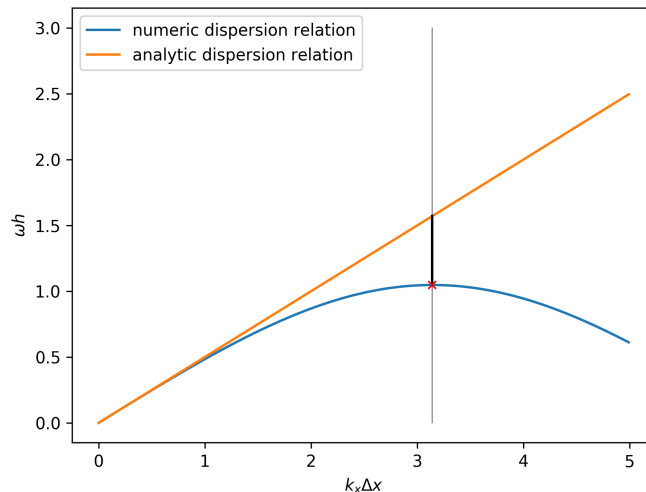


Figure 4.2.: Comparison of numerical and analytical dispersion relation of discretized Maxwell Equations with Yee Scheme. We used $c \equiv 1$ and $\frac{\Delta t}{\Delta x} \equiv \frac{1}{2}$. At $\tilde{k}_x^{max} = \frac{\pi}{\Delta x}$ the group velocity vanishes instead of propagating with speed of light. Therefore, only waves with $\lambda \ll \lambda^{max}$ can be resolved properly on the grid.

After having discussed the fundamentals, we now want to dive into practice. In Section 4.1 we learned how to store and propagate the fields on a numerical grid. In Section 1.3 we derived an analytical expression, of how to calculate the fields of a moving charged particle. We also observed that there is a singularity in (1.32) at the particle position itself. That means, that the fields will vary strongly in a vicinity of the particle and can not be resolved correctly on the grid, as discussed in Section 4.2. Hence, it seems plausible to separate the simulation area into appropriate Near - and far field areas. Within the near field area of a particle, its fields will **not** be stored on the grid. We then do not need to worry about the singularity. Only far fields from other particles, propagated into the near field area will be further propagated and stored on the grid. Possible interactions with other particles within the near field area will be calculated analytically from (1.32). far fields will be stored on the grid and propagated with the Yee-Scheme (4.1).

4.3 Near-and Far Fields

Before we can separate the simulation area into Near - and far fields, we need to initialize a grid. We divide the grid in `numberBoxesInX`, `numberBoxesInY` and `numberBoxesInZ` boxes, each of which has `numberOfGridPointsForBoxInX`, `numberOfGridPointsForBoxInY` and `numberOfGridPointsForBoxInZ` length, which leaves us with a total

```
numberOfGridPointsInX = numberOfGridPointsForBoxInX * numberBoxesInX;
numberOfGridPointsInY = numberOfGridPointsForBoxInY * numberBoxesInY;
numberOfGridPointsInZ = numberOfGridPointsForBoxInZ * numberBoxesInZ;
```

Upon defining the resolution `dx`, `dy`, `dz` the size of the simulation area is then given by

```
lengthOfSimulationBoxInX = numberOfGridPointsInX * dx;
lengthOfSimulationBoxInY = numberOfGridPointsInY * dy;
lengthOfSimulationBoxInZ = numberOfGridPointsInZ * dz;
```

The near field is then defined as the $3 \cdot 3 \cdot 3 = 27$ boxes with the box, containing the particle, in the center. In Figure 4.3 the near fields of one and two particles are shown. The near fields can of course overlap. The near field box at (18, 18) belongs to both particles.

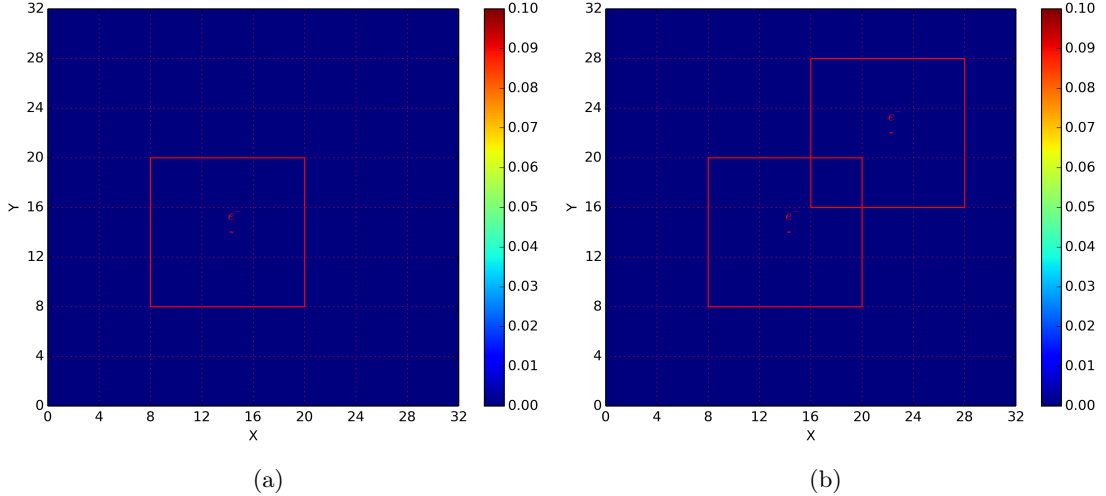


Figure 4.3.: near fields of one (a) and two (b) particles. The box at (18, 18) belongs to the near field of both particles, marked with e^- . Notice the staggered red grid in the background. In this example we used 8 boxes, with 20 grid points each, and a resolution of $dx = dy = dz = 0.2$. The plotted plane was chosen accordingly to the z - coordinate of the particle.

4.4 Field Push

We now want to explain, how a field push actually works. Since we only propagate fields in the far field area as explained in Section 4.1 special care needs to be taken at the boundaries between far field and near field. To explain this, consider the following plane of a grid illustrated in Figure 4.4. The red dots are considered to be the near field area of a particle. The black dots are therefore the far field area. The grid points within the near field does not contain any field values. We only store and propagate fields on the grid points in the far field. If we now want to push the value for H_z at $(2, 4, k)$ (recall that each grid point contains the field values for either H_x , H_y , H_z or E_x , E_y , E_z due to the staggered grid, explained in Section 4.1), where $k \in (1, 2, 3, \dots, \text{numberOfGridPointsInZ} - 1)$, we need to solve

$$\frac{\partial H_z}{\partial t} = - \left(\frac{\partial E_y}{\partial x} - \frac{\partial E_x}{\partial y} \right). \quad (4.15)$$

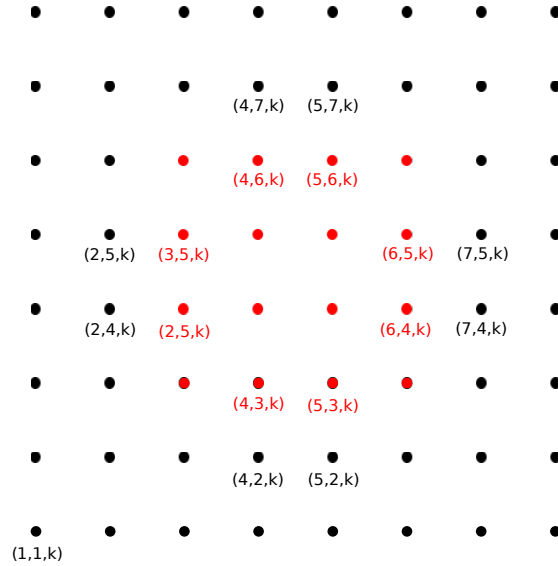


Figure 4.4.: One plane of a grid showing the **near field** and far field of a particle. The **near field** does not contain any field values of the particle. k denotes the plane at an height z and can be chosen arbitrarily here.

Using the discretized Maxwell Equations (4.1) we get

$$\vec{H}\Big|_{z(2,4,k)}^{n+1} = \vec{H}\Big|_{z(2,4,k)}^n - h \left(\frac{\vec{E}\Big|_{y(3,4,k)}^{n+\frac{1}{2}} - \vec{E}\Big|_{y(2,4,k)}^{n+\frac{1}{2}}}{\Delta x} - \frac{\vec{E}\Big|_{x(2,5,k)}^{n+\frac{1}{2}} - \vec{E}\Big|_{y(2,4,k)}^{n+\frac{1}{2}}}{\Delta y} \right). \quad (4.16)$$

$\vec{H}\Big|_{z(2,4,k)}^{n+1}$ is stored on a far field grid point. Its calculation, however, requires a field value $\vec{E}\Big|_{y(3,4,k)}^{n+\frac{1}{2}}$, which is stored on a near field grid point and therefore contains no field values from the particle (it can, however, contain field values from other particles propagated from the outside into the near field area). Hence, we need to analytically calculate the Liénard-Wiechert field (1.32) of the particle at $(3, 4, k)$ $\vec{E}\Big|_{yp(3,4,k)}^{n+\frac{1}{2}}$ and add it to the field

value already stored at this grid point. Finally, the correct calculation is

$$\vec{H}|_{z(2,4,k)}^{n+1} = \vec{H}|_{z(2,4,k)}^n - h \left(\frac{\left(E|_{y(3,4,k)}^{n+\frac{1}{2}} + E|_{yp(3,4,k)}^{n+\frac{1}{2}} \right) - E|_{y(2,4,k)}^{n+\frac{1}{2}}}{\Delta x} - \frac{E|_{x(2,5,k)}^{n+\frac{1}{2}} - E|_{y(2,4,k)}^{n+\frac{1}{2}}}{\Delta y} \right). \quad (4.17)$$

On the contrary, if we want to push the value for H_z at $(6, 4, k)$ we need to analytically calculate the Liénard-Wiechert field (1.32) of the particle at $(7, 4, k)$ $E|_{yp(7,4,k)}^{n+\frac{1}{2}}$ and subtract it from the field value already stored at this grid point. $(7, 4, k)$ already contains the field contribution of the particle, since it is a far field grid point. And because $(6, 4, k)$ is a near field grid point we only want to take contributions from other particles into account, which are about to propagate into our near field area. After subtracting the particles own contributions, the correct push can be calculated via

$$\vec{H}|_{z(6,4,k)}^{n+1} = \vec{H}|_{z(6,4,k)}^n - h \left(\frac{\left(E|_{y(7,4,k)}^{n+\frac{1}{2}} - E|_{yp(7,4,k)}^{n+\frac{1}{2}} \right) - E|_{y(6,4,k)}^{n+\frac{1}{2}}}{\Delta x} - \frac{E|_{x(6,5,k)}^{n+\frac{1}{2}} - E|_{y(6,4,k)}^{n+\frac{1}{2}}}{\Delta y} \right). \quad (4.18)$$

This and more examples as well as a more detailed explanation can be found in [12]. All points along the border between near - and far field need to be adjusted accordingly.

We now want to explain how this works out in code. Figure 4.5 shows three boxes, two of which are near field boxes and one is a far field box. For reasons of clarity we only show the grid points along the edges.

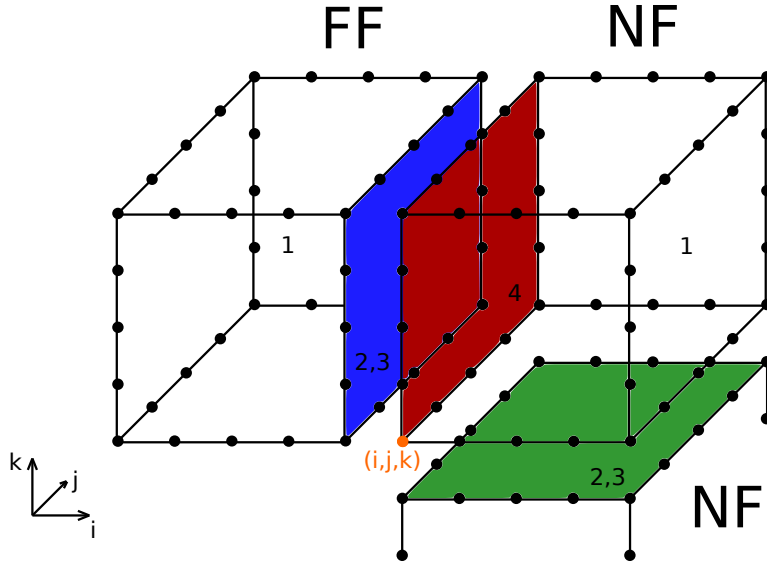


Figure 4.5.: Section of a grid with three boxes, two of which are near field boxes (NF) and one being a far field box (FF). The colored planes represent those grid points, where adjustments are necessary, as explained above. One \vec{E} - Field push consists of four steps, or equivalently four subroutines in code: 1. `pushEFieldInsideBoxes`, 2. `setHFieldOnBorders`, 3. `adjustHFields`, 4. `pushEFieldAtBorders`. For reasons of clarity we left out the grid points within the boxes.

One complete field push consists out of four steps. Even though the field pushes for \vec{H} and \vec{E} are conceptionally identical, they differ in the grid points they are accessing to calculate the rotations $\vec{\nabla}^+$ and $\vec{\nabla}^-$ in (4.1). The steps (subroutines) for one \vec{E} - Field push are

1. `pushEFieldInsideBoxes()`
2. `setHFieldOnBorders()`
3. `adjustHField()`
4. `pushEFieldOnBorders()`

Since this is the core of the simulation, these steps will be explained in more detail below.

4.4.1 `pushEFieldInsideBoxes()`

In this routine we simply calculate the discretized Maxwell Equations (4.1). We loop through the entire grid and store the necessary field values but leave out those grid points which are on the left plane (yz -plane) of each box. In Figure 4.5 marked with red.

Now all \vec{E} values in all boxes are pushed except those on the red plane. To push those we need to access the field values on the blue and green plane, which are in the far field and therefore need to be adjusted.

4.4.2 `setHFieldOnBorders()`

In order to push \vec{E} we need values of \vec{H} . Therefore, this method loops through all boxes and stores all values of \vec{H} in the plane left, in front and below of the current box (the plane in front is not shown for reasons of clarity). As can be seen from the Yee Scheme only Hy and Hz are needed from the left plane. Hz and Hx are needed from the plane in front and Hy and Hx are needed from the plane below. If the current box is a box where to the left does not exist then the respective values for H are set to zero.

4.4.3 `adjustHField()`

This routine consists of three subroutines `adjustHyz_im1()`, `adjustHxz_jm1()` and `adjustHxy_km1()`. The first adjusts Hy and Hz on plane to the left, the second adjusts Hx and Hz on the plane in front (not shown) and the latter adjusts Hx and Hy on the plane below. All of those three subroutines do conceptionally the same. They loop through all boxes and check whether the current box is part of the near field of the particle and the box to the left is not. This is the situation shown in Figure 4.5. Then the respective Liénard-Wiechert fields get calculated on the blue plane and subtracted from the values stored by `setHFieldOnBorders()`. Notice that the red plane is part of a near field box and the blue plane is part of a far field box. Hence, we need to subtract the field contributions of the particle on the blue plane.

On the contrary, if we have the case that the current box is a far field box and the box to left is a near field box, then the red plane is part of a far field box and the blue plane is part of a near field box. Hence, we calculate the Liénard-Wiechert fields on the blue plane and add them to the respective values stored by `setHFieldOnBorders()`.

4.4.4 `pushEFieldOnBorders()`

This method finally pushes the \vec{E} - Field with the adjusted values. It also loops through the entire grid, but only gets active if the current grid point lies on the red plane. If so, then it gets the values stored by `setHFieldOnBorders()` and adjusted by `adjustHField()`

and uses them to calculate the discretized Maxwell Equation (4.1).

The routines for pushing the \vec{H} - Field are analogously:

1. `pushHFieldInsideBoxes()`
2. `setEFieldOnBorders()`
3. `adjustEField()`
4. `pushHFieldOnBorders()`

while using the planes to the right, behind and above.

As an example we simulate an electron with $\gamma = 1.1$ in a constant external B_z field. Figure 4.6 shows the result.

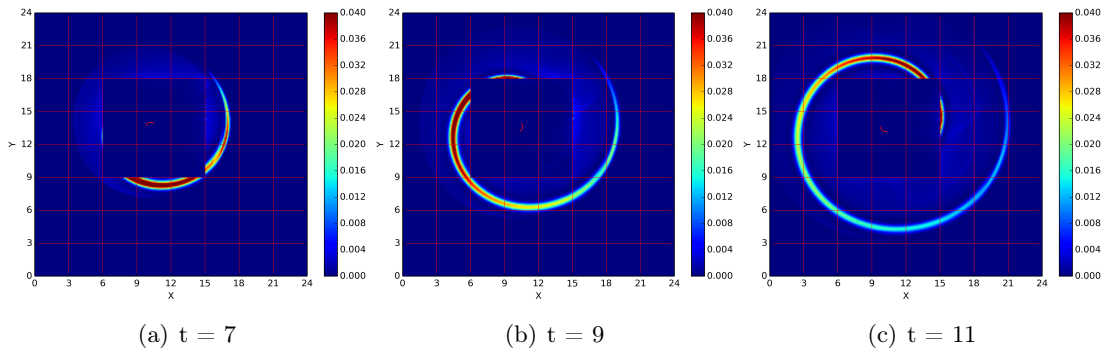


Figure 4.6.: Simulation of an electron with $\gamma = 1.1$ in a constant $B_z = 1$ field. The colorbar shows the value of $|\vec{E}|^2$. \vec{E} and $c\vec{B}$ are in units of $4\pi\epsilon_0 m_e^2 c^4/e^3 = 1.77 \cdot 10^{20} \text{V m}^{-1}$, length in units of $e^2/(4\pi\epsilon_0 m_e c^2) = 2.82 \cdot 10^{-15} \text{m}$ and times in units of $e^2/(4\pi\epsilon_0 m_e c^3) = 9.40 \cdot 10^{-24} \text{s}$.

The electron moves in a circular fashion in the xy - plane. The red line in the center of the near field area shows the particles trajectory. The initial conditions are chosen such that the particle does not leave its initial box. That means that the near field does not change during runtime. The Liénard-Wiechert fields are only calculated at the border between near - and far field and only if the retardation constraint $t_{ret} > 0$ is met.

As we already mentioned before, Figure 4.7 finally shows the expected behavior of two particle's far fields propagating into each other's near field regions.

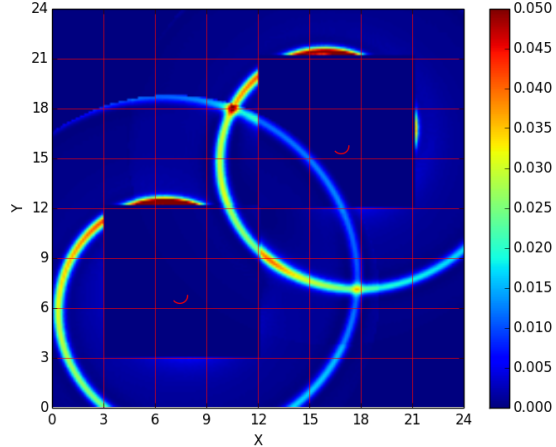


Figure 4.7.: Gyration of two electrons with $\gamma = 1.1$ each. This shows the expected behavior of two particle's far fields propagating into each other's near field regions. The colorbar shows the value of $|\vec{E}|^2$. \vec{E} and $c\vec{B}$ are in units of $4\pi\epsilon_0 m_e^2 c^4/e^3 = 1.77 \cdot 10^{20} \text{ V m}^{-1}$ and length in units of $e^2/(4\pi\epsilon_0 m_e c^2) = 2.82 \cdot 10^{-15} \text{ m}$.

But what if the particle does leave its initial box ?

4.5 Particle Push and Near Field Update

In order to push the particle properly not just the external fields but also the field contributions from other particles propagated into the near field region need to be taken into account. To get an even better result we use trilinear interpolation (see Section 3.2) to interpolate the field value at the particle position from the surrounding eight grid points. If, however, another particle2 enters the near field region of the observed particle1 equation (1.32) is used to calculate the field emitted by particle2 at the position of particle1 analytically.

If a particle changes its box during one push from time t to $t + dt$ the particles near field changes as illustrated in Figure 4.8

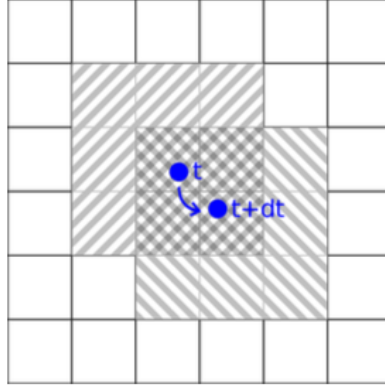


Figure 4.8.: Particle push from time t to $t+dt$. Since the particle changes its box the near field region also changes. The boxes marked with \diagup do no longer belong to the near field, whereas the boxes marked with \diagdown do now belong to the near field area. Boxes illustrated as \blacksquare remain as near field boxes. [12]

There are three situations we need to take care of. First the boxes which do not longer belong to the near field area, marked with \diagup in Figure 4.8. Since those boxes were part of the near field they didn't contain any field contributions of the particle. But because they are no longer part of the near field region those field contributions need to be added. The routine `addLWFieldsInBox()` calculates the Liénard-Wiechert field (1.32) of the particle at all grid points in the specified box and adds them to the respective grid point. Second, all boxes marked with \diagdown are now part of the near field region and therefore the Liénard-Wiechert field of the particle at all grid points in the specified box need to be subtracted. The routine `subLWFieldsInBox()` does exactly that. Lastly, there are boxes which remain as part of the near field area marked with \blacksquare . Nothing needs to be done here.

As an example we simulate an electron with $\gamma = 1.2$ in a crossed \vec{E} and \vec{B} field. The results are shown in Figure 4.9

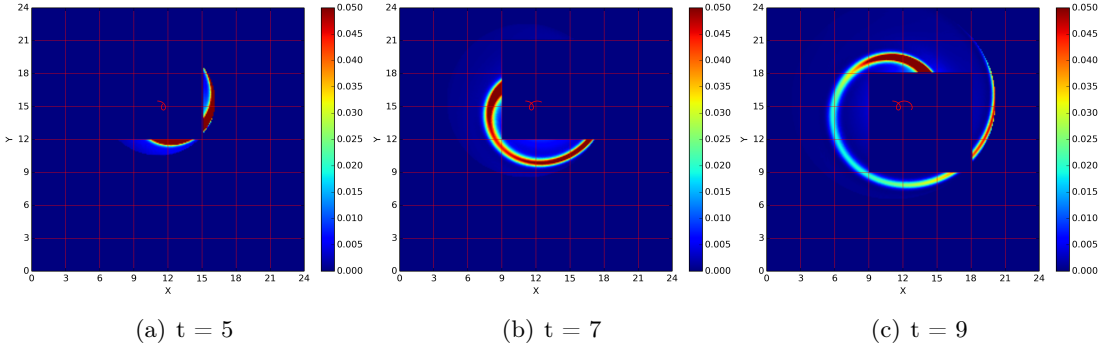


Figure 4.9.: Simulation of an electron with $\gamma = 1.2$ in a crossed electromagnetic field with $B_z = 1$ and $E_y = 0.2$. The colorbar shows the value of $|\vec{E}|^2$. \vec{E} and $c\vec{B}$ are in units of $4\pi\epsilon_0 m_e^2 c^4 / e^3 = 1.77 \cdot 10^{20} \text{ V m}^{-1}$, length in units of $e^2 / (4\pi\epsilon_0 m_e c^2) = 2.82 \cdot 10^{-15} \text{ m}$ and times in units of $e^2 / (4\pi\epsilon_0 m_e c^3) = 9.40 \cdot 10^{-24} \text{ s}$

4.6 Particle History

In order to calculate the Liénard-Wiechert Field according to (1.32) at an observation point, i.e. a grid point, the intersection point of the particles trajectory with the backward lightcone of that observation point is needed. For a more detailed explanation see Section 3.1. That means, that we first have to store all positions of the particle. Second we need to track them along the trajectory to check whether the backward lightcone was crossed or not. To store the entire trajectory of a few particles is not very memory consuming. However, if we want to simulate 10^{10} or even 10^{20} particles we would need a huge amount of memory just to store the trajectories. Let's do a rough calculation: One position contains of four Doubles. One for time, three for spacial components. A Double has 8 B. That makes a total of 32 B memory for one particle position. If we want to simulate for $t = 10$ with a resolution of $dx = dy = dz = 0.1$ using Yee-Scheme we will have $\frac{10}{0.5 \cdot 0.1} = 200$ steps. That gives us $200 \cdot 32 \text{ B} = 6.4 \text{ kB}$. For 10^{10} particles this sums up to 64 TB. This is not feasible! Not to mention that there is a lot more memory necessary to store all the calculated fields on the grid.

The problem is that we can't simply delete the positions we already used to find an intersection point, because the intersection point depends on the particles velocity. The faster the particle gets, the longer the history needs to be. We can see why that is in the following picture 4.10

CHAPTER 4. HYBRID FIELD APPROACH

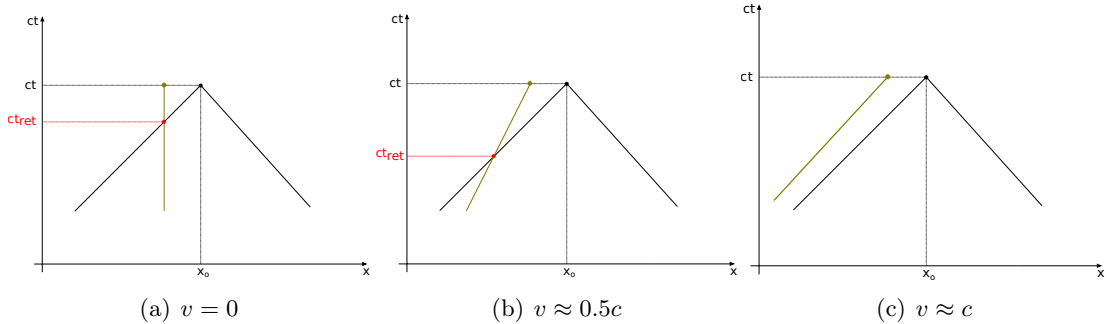


Figure 4.10.: Observation point x_o at time ct . The particle trajectory is shown in ochre.

The intersection point is marked red. We can see that the faster the particle gets the longer the particle history needs to be in order to find the intersection point. At the speed of light there would be no intersection point, since the backward lightcone and the particle history would be parallel.

We see an observation point x_o and its backward lightcone in a Minkowsky Space. The ocher line illustrates the particles trajectory, crossing the backward lightcone at an intersection point, marked as red dot. With increasing velocity the trajectory tends more and more towards a 45° angle. At $v = c$ the trajectory would be parallel to the backward lightcone and thus an intersection would be impossible. Therefore, we can conclude that a plausible criteria for finding the position after which all following positions could be neglected has to be velocity dependent. Due to the aforementioned arguments we can moreover conclude that the dependence would be proportional to $\frac{1}{1-\beta}$. But this is not good enough. Since the velocity can change during runtime, we need an a priori approach to reduce the memory consumption. As discussed in Section 1.3.3 we know that the intensity declines with a $\frac{1}{r^2}$ dependance. This allows us to define a distance over which the emitted fields would be attenuate so much, that they could be neglected. Unfortunately we were not able to develop a concrete formulation of that idea, yet. So we have not implemented and tested it so far.

4.7 Far Field Setup Before Simulation

So far we can initialize a particle (or multiple particles) and let them move on the grid according to the Lorentz-Newton equation (2.1) without damping. If there are external fields or interaction forces between multiple particles they get accelerated and start to radiate Liénard-Wiechert fields. As soon as the retardation constraint is met ($t_{ret} > 0$) the fields will appear at the border between near - and far field region and get propagated via (4.1). This works fine, but unfortunately this initial setup is far from realistic. The particles were not created the second the simulation starts. We are not interested in simulating the creational process but the emitted fields due to interactions between particles which do already exist. Therefore, the particles will already have a long trajectory history and some kind of Liénard-Wiechert fields coming with them. So, the question is: How do we setup the fields on the grid before the simulation starts ? We use the following approach:

We use the Boris-Pusher (see Section 2.3.1) to push the particles from t to $t + dt$, starting with the initial conditions, given prior to the simulation. This algorithm can also be used to push backwards in time, since it is symplectic and therefore time reversible. By selecting the simulation parameter $t = t_0 > 0$ the trajectory will be calculated backwards in time for t_0 time units. This can be achieved by reversing the external fields and the initial velocity vector of the particle. Once we got t_0 back in time, we reverse the external fields and the velocity vector again, set the particles proper time to zero and start pushing the particle from there. In order to store all new trajectory points in the history, it needs to be extended by $\frac{t_0}{dt}$ elements first. With this approach the simulation starts with the particle being at the specified initial conditions by the user, but the particle will already have a trajectory history, from which the initial Liénard-Wiechert fields can be calculated with (1.32) in all far field boxes of the grid. This, however, is computationally quite expensive. We therefore developed a routine which serializes the initial conditions of the simulation in a file and only calculates the fields if they were not calculated and stored before. The flow chart in Figure 4.12 shows which functions get called when the user sets $t = t_0 > 0$. In Figure 4.11 some examples of initial fields for different times are shown. Notice that in all cases the simulation starts with the particle being at the initial position ¹ the user entered prior to the simulation. Only the distance over which the fields are initialized differ due to different particle history length.

¹Particle->x[1] = 11.1
Particle->x[2] = 15.5

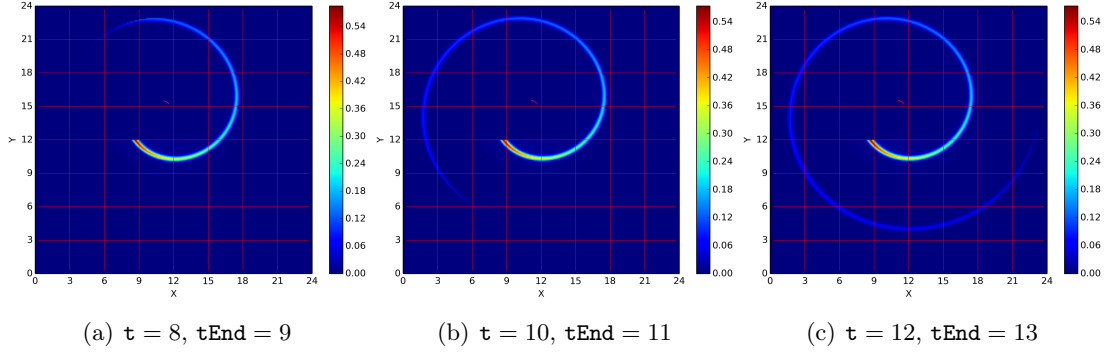


Figure 4.11.: Initial fields for different values of simulation parameter t . If $t > 0$ the history gets extended with a reverse Boris Push such that the initial conditions are still met at the beginning of the simulation. The Liénard-Wiechert fields are calculated from the extended particle history.

The electron has an energy of $\gamma = 1.2$. We used a constant $B_z = 1$ as external field. The colorbar shows the value of $|\vec{E}|^2$. \vec{E} and $c\vec{B}$ are in units of $4\pi\epsilon_0 m_e^2 c^4 / e^3 = 1.77 \cdot 10^{20} \text{ V m}^{-1}$, length in units of $e^2 / (4\pi\epsilon_0 m_e c^2) = 2.82 \cdot 10^{-15} \text{ m}$ and times in units of $e^2 / (4\pi\epsilon_0 m_e c^3) = 9.40 \cdot 10^{-24} \text{ s}$

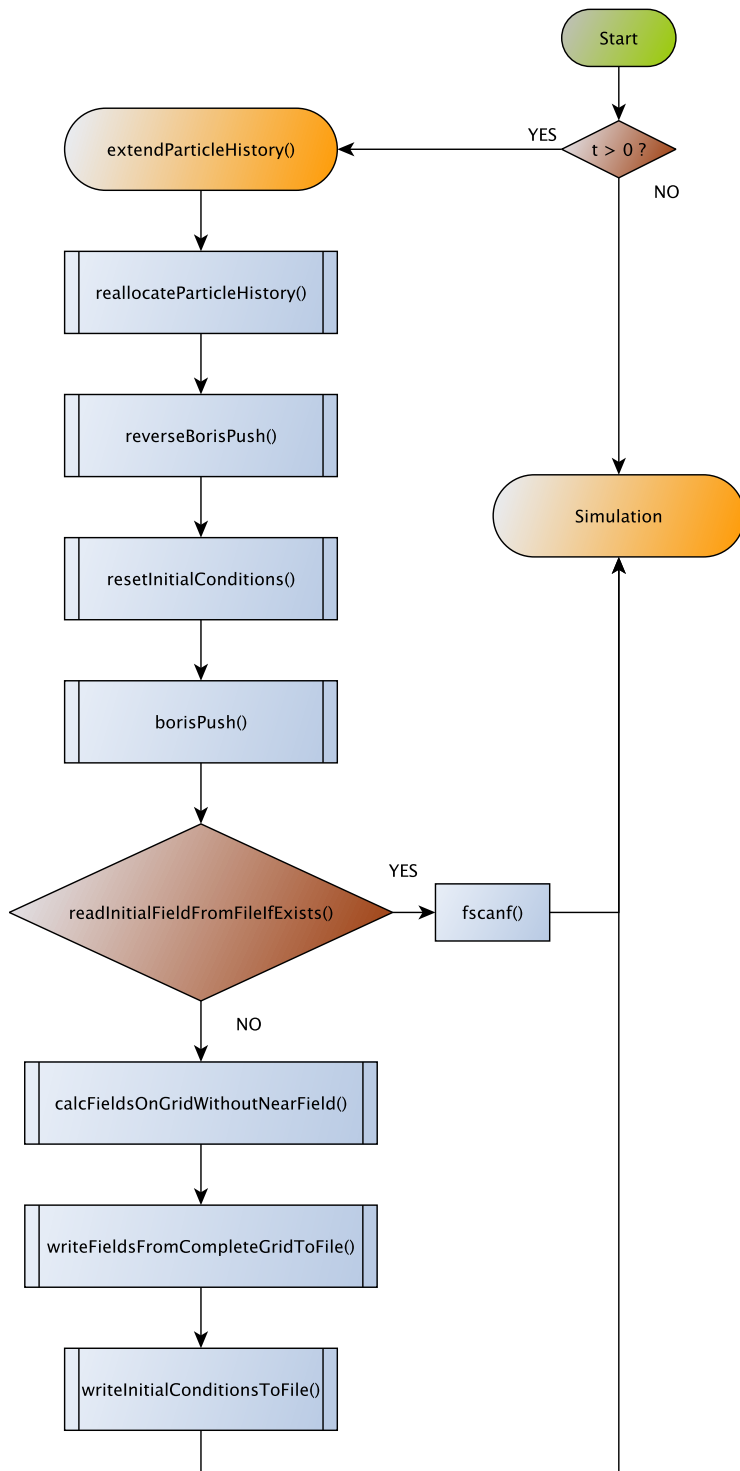


Figure 4.12.: Flow Chart showing the relevant function calls when the user sets $t = t_0 > 0$. If $t = t_0 = 0$ the simulation starts right away.

4.8 Electron Scattering in an electromagnetic wave

Finally, to proof the framework's proper functionality, an electron scattering process with a laser pulse shall be simulated, which could be reproduced in the lab. Due to the normalization (see Appendix D) the scales need to be adapted in order to have realistic scales. For instance, the ratio of the normalized characteristic frequency ω to the laser frequency ω_L needs to be calculated first. We also need to find the ratio of the normalized electric field amplitude E_0 to the laser electric field amplitude E_{0L} and also a proper time resolution. In the following we present a rough estimate of the aforementioned quantities.

In order to find $\frac{\omega_L}{\omega}$ we start with the laser amplitude a_0 , which us usually of the order

$$a_0 = \frac{eE_{0L}}{m_e\omega_L c} = 100. \quad (4.19)$$

Typical laser wavelengths are of the order

$$\begin{aligned} \lambda_L &= 10^{-6} \text{m} = 1 \mu\text{m} \\ \implies \nu_L &= \frac{c}{\lambda_L} \approx 3 \cdot 10^{14} \text{s}^{-1} \\ \implies \omega_L &= 2\pi\nu_L = 1.88 \cdot 10^{15} \text{s}^{-1}. \end{aligned} \quad (4.20)$$

Since

$$\omega = \frac{4\pi\epsilon_0 m_e c^3}{q^2} = 1.06 \cdot 10^{23} \text{s}^{-1} \quad (4.21)$$

we find

$$\frac{\omega_L}{\omega} = 1.77 \cdot 10^{-8} \text{s}^{-1}. \quad (4.22)$$

Using the relationship between ω_L and ω we can find

$$\begin{aligned} E_{0L} &\equiv \frac{a_0 m_e \omega_L c}{q} \\ &= 100 \frac{m_e c}{q} \cdot 1.77 \cdot 10^{-8} \frac{4\pi\epsilon_0 m_e c^3}{q^2} \\ &= 1.77 \cdot 10^{-6} \frac{4\pi\epsilon_0 m_e^2 c^4}{q^3} \\ &= 1.77 \cdot 10^{-6} E_0. \end{aligned} \quad (4.23)$$

The same holds for B_{0L} . Finally, we need to determine the grid resolution dx and therefore dt . In order to resolve the fields properly on the grid, the time resolution needs to be so small that

$$\Delta t_L \omega_L \ll 1 \quad (4.24)$$

holds. Plugging in yields

$$\Delta t_L \ll \frac{1}{\omega_L} \stackrel{(4.22)}{=} \frac{1}{1.77 \cdot 10^{-8} \omega} = 1.77 \cdot 10^8 t. \quad (4.25)$$

Since $dt = 0.5dx$ (see Section 4.1) choosing $dx = 10^7$ is sufficiently small.

For the upcoming results the following settings were used

```

Resolution->dx = pow(10, 7);
Resolution->dy = pow(10, 7);
Resolution->dz = pow(10, 7);

Box->numberOfGridPointsInX = 32;
Box->numberOfGridPointsInY = 32;
Box->numberOfGridPointsInZ = 32;

Grid->numberOfBoxesInX = 22;
Grid->numberOfBoxesInY = 10;
Grid->numberOfBoxesInZ = 10;

int numberOfParticles = 1;

double dt = 0.5 * Resolution.dx;
double t = 400 * pow(10, 7);
double tEnd = 1100 * pow(10, 7);

Particle1->mass = pow(10, 10);
Particle1->charge = pow(10, 10);

Particle1->x[0] = 0;
Particle1->x[1] = 6.0 * pow(10, 9);
Particle1->x[2] = 1.6 * pow(10, 9);
Particle1->x[3] = 1.6 * pow(10, 9);

```

For the external laser pulse we modulated a cosine function with a sin squared function in x direction and a gaussian in y direction. Figure 4.13 shows the external pulse.

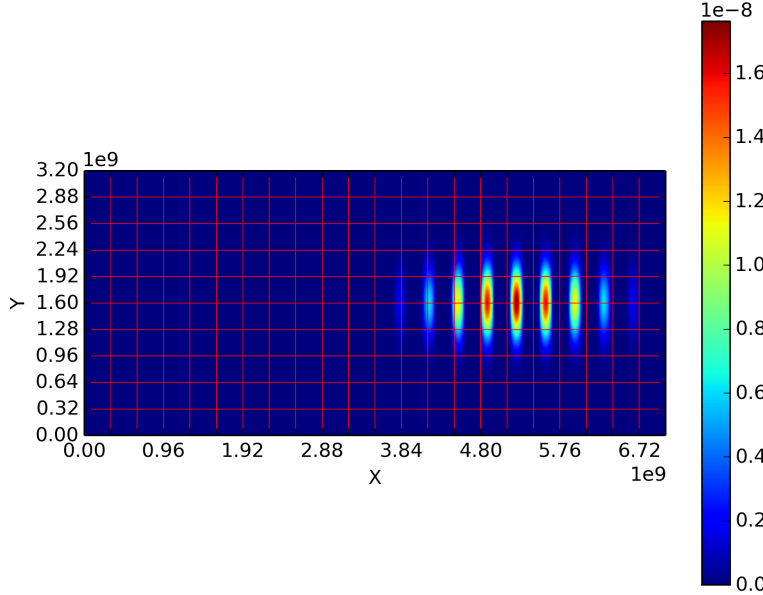


Figure 4.13.: External laser pulse at $t = 700$. The colorbar shows the value of $|\vec{E}|^2$. \vec{E} and $c\vec{B}$ are in units of $4\pi\epsilon_0 m_e^2 c^4 / e^3 = 1.77 \cdot 10^{20} \text{ V m}^{-1}$, length in units of $e^2 / (4\pi\epsilon_0 m_e c^2) = 2.82 \cdot 10^{-15} \text{ m}$ and times in units of $e^2 / (4\pi\epsilon_0 m_e c^3) = 9.40 \cdot 10^{-24} \text{ s}$.

The idea is to slowly increase γ while maintaining a small angle between the particle and the incoming external laser pulse. With increasing γ the direction of the radiated Linard Wiéchert field should become more more directed. Similarly, the radiation frequency should increase as well. Using increments of $\Delta\gamma = 0.1$ we increased from $\gamma = 1.0$ up to $\gamma = 1.5$. To analyze the radiation direction and radiation frequency we made a Fourier Analysis of the electric field components \vec{E} and of the components of the Poynting vector \vec{S} . Figures 4.14 - 4.25 show the plain simulation results, both with and without the near field region of the particle. The ratio of damping Force g^μ and Lorentz force was also calculated at each time step. This way it is easy to show that the damping term g^μ can be neglected.

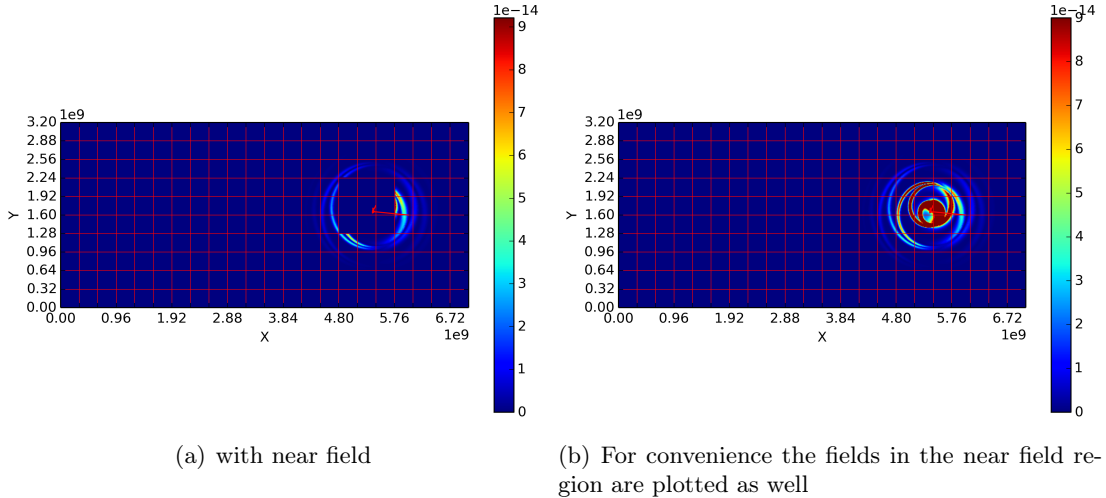
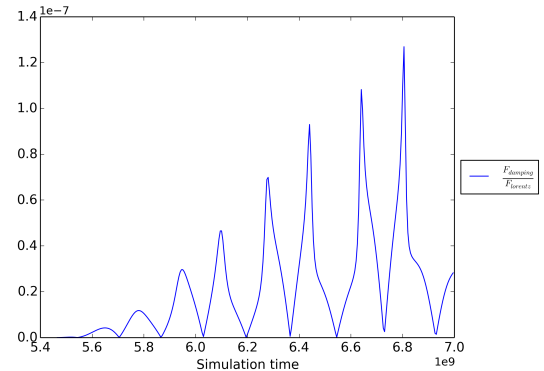


Figure 4.14.: Initial Conditions: `Particle1->u[1] = 0.1`, `Particle1->u[2] = 0.01` and `Particle1->u[3] = 0.0`. The particle history is calculated for $t = 400 * \text{pow}(10, 7)$ prior to the simulation. The pictures are taken at $t = 1100 * \text{pow}(10, 7)$.

The electron has an energy of $\gamma = 1.0$. We used the external pulse from above as external field and is therefore not shown here. The colorbar shows the value of $|\vec{E}|^2$. \vec{E} and $c\vec{B}$ are in units of $4\pi\epsilon_0 m_e^2 c^4 / e^3 = 1.77 \cdot 10^{20} \text{ V m}^{-1}$, length in units of $e^2 / (4\pi\epsilon_0 m_e c^2) = 2.82 \cdot 10^{-15} \text{ m}$ and times in units of $e^2 / (4\pi\epsilon_0 m_e c^3) = 9.40 \cdot 10^{-24} \text{ s}$.

Figure 4.15: Ratio of the damping force g^μ and Lorentz force F_L at $\gamma = 1.0$. g^μ was calculated at each time step according to (2.3). Obviously, the damping term g^μ can be neglected. Time is in units of $e^2 / (4\pi\epsilon_0 m_e c^3) = 9.40 \cdot 10^{-24} \text{ s}$.



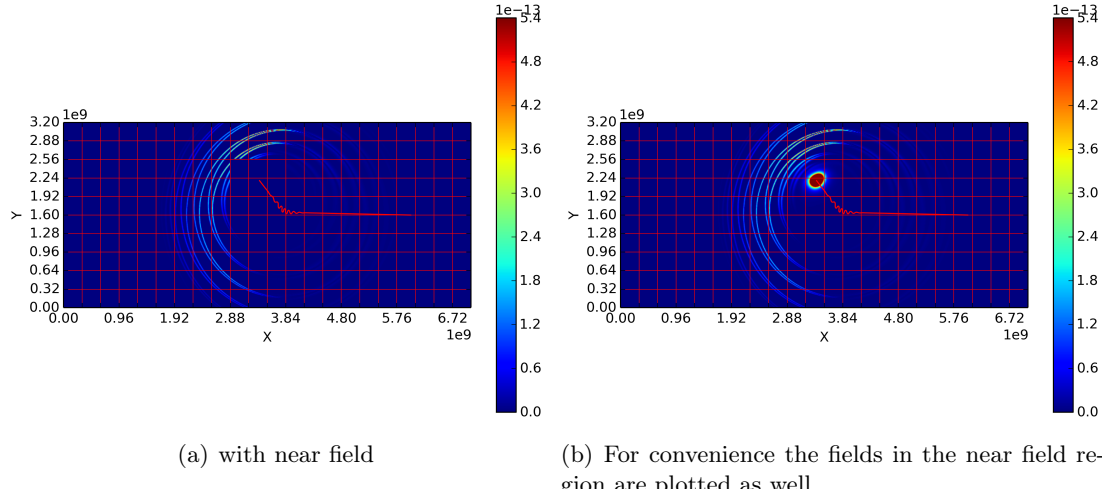


Figure 4.16.: Initial Conditions: `Particle1->u[1] = 0.46`, `Particle1->u[2] = 0.01` and `Particle1->u[3] = 0.0`. The particle history is calculated for $t = 400 * \text{pow}(10, 7)$ prior to the simulation. The pictures are taken at $t = 1100 * \text{pow}(10, 7)$.

The electron has an energy of $\gamma = 1.1$. We used the external pulse from above as external field and is therefore not shown here. The colorbar shows the value of $|\vec{E}|^2$. \vec{E} and $c\vec{B}$ are in units of $4\pi\epsilon_0 m_e^2 c^4/e^3 = 1.77 \cdot 10^{20} \text{ V m}^{-1}$, length in units of $e^2/(4\pi\epsilon_0 m_e c^2) = 2.82 \cdot 10^{-15} \text{ m}$ and times in units of $e^2/(4\pi\epsilon_0 m_e c^3) = 9.40 \cdot 10^{-24} \text{ s}$.

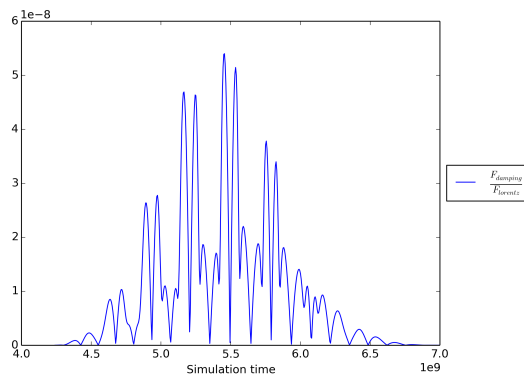


Figure 4.17: Ratio of the damping force g^μ and Lorentz force F_L at $\gamma = 1.1$. g^μ was calculated at each time step according to (2.3). Obviously, the damping term g^μ can be neglected. Time is in units of $e^2/(4\pi\epsilon_0 m_e c^3) = 9.40 \cdot 10^{-24} \text{ s}$.

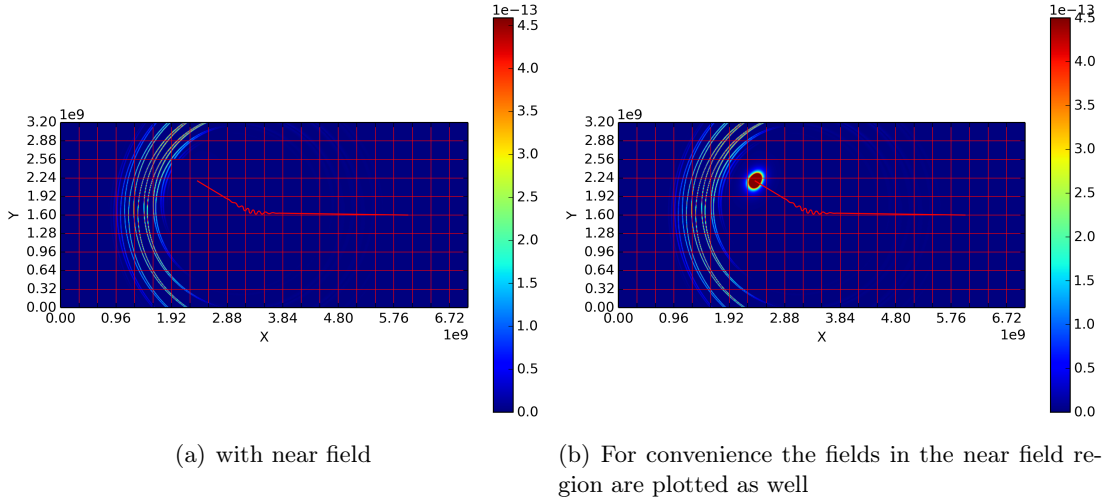
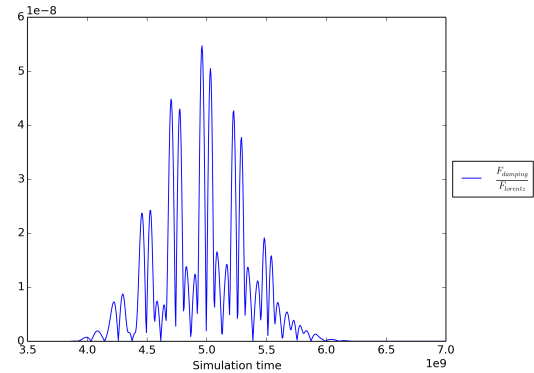


Figure 4.18.: Initial Conditions: $\text{Particle1-}u[1] = 0.67$, $\text{Particle1-}u[2] = 0.01$ and $\text{Particle1-}u[3] = 0.0$. The particle history is calculated for $t = 400 * \text{pow}(10, 7)$ prior to the simulation. The pictures are taken at $t = 1100 * \text{pow}(10, 7)$.

The electron has an energy of $\gamma = 1.2$. We used the external pulse from above as external field and is therefore not shown here. The colorbar shows the value of $|\vec{E}|^2$. \vec{E} and $c\vec{B}$ are in units of $4\pi\epsilon_0 m_e^2 c^4/e^3 = 1.77 \cdot 10^{20} \text{ V m}^{-1}$, length in units of $e^2/(4\pi\epsilon_0 m_e c^2) = 2.82 \cdot 10^{-15} \text{ m}$ and times in units of $e^2/(4\pi\epsilon_0 m_e c^3) = 9.40 \cdot 10^{-24} \text{ s}$.

Figure 4.19: Ratio of the damping force g^μ and Lorentz force F_L at $\gamma = 1.2$. g^μ was calculated at each time step according to (2.3). Obviously, the damping term g^μ can be neglected. Time is in units of $e^2/(4\pi\epsilon_0 m_e c^3) = 9.40 \cdot 10^{-24} \text{ s}$.



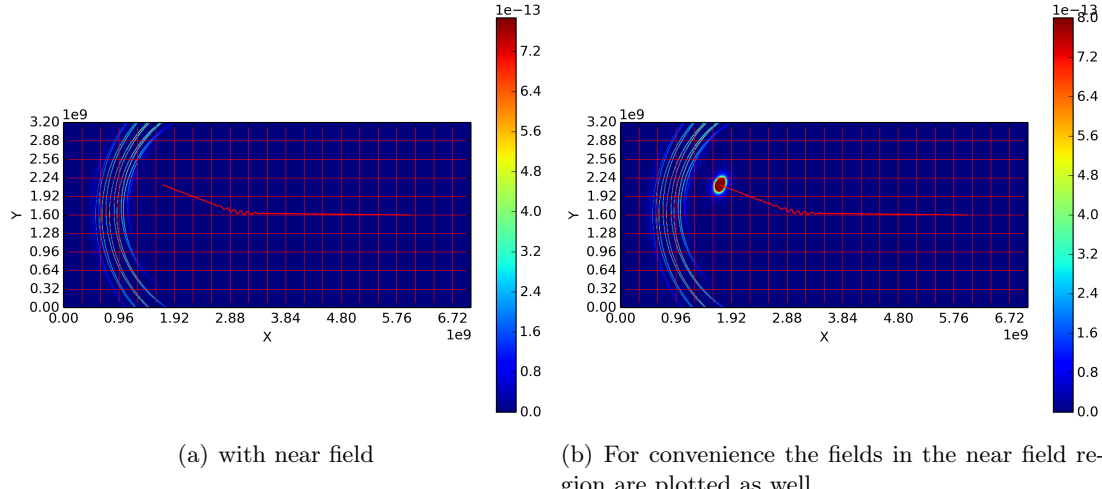


Figure 4.20.: Initial Conditions: `Particle1->u[1] = 0.84`, `Particle1->u[2] = 0.01` and `Particle1->u[3] = 0.0`. The particle history is calculated for $t = 400 * \text{pow}(10, 7)$ prior to the simulation. The pictures are taken at $t = 1100 * \text{pow}(10, 7)$.

The electron has an energy of $\gamma = 1.3$. We used the external pulse from above as external field and is therefore not shown here. The colorbar shows the value of $|\vec{E}|^2$. \vec{E} and $c\vec{B}$ are in units of $4\pi\epsilon_0 m_e^2 c^4/e^3 = 1.77 \cdot 10^{20} \text{ V m}^{-1}$, length in units of $e^2/(4\pi\epsilon_0 m_e c^2) = 2.82 \cdot 10^{-15} \text{ m}$ and times in units of $e^2/(4\pi\epsilon_0 m_e c^3) = 9.40 \cdot 10^{-24} \text{ s}$.

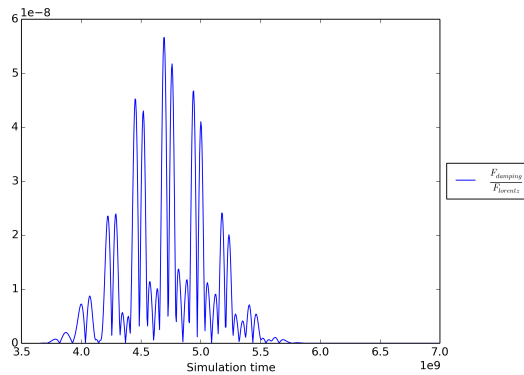


Figure 4.21: Ratio of the damping force g^μ and Lorentz force F_L at $\gamma = 1.3$. g^μ was calculated at each time step according to (2.3). Obviously, the damping term g^μ can be neglected. Time is in units of $e^2/(4\pi\epsilon_0 m_e c^3) = 9.40 \cdot 10^{-24} \text{ s}$.

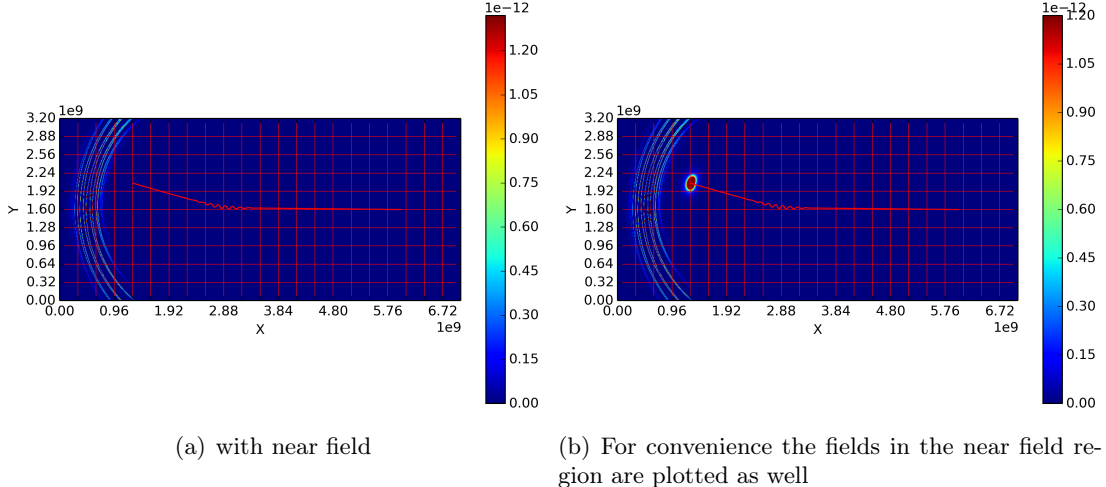
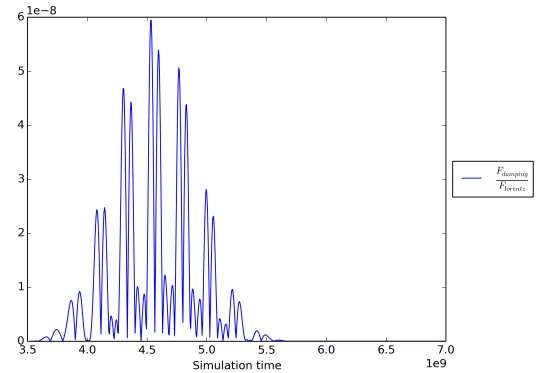


Figure 4.22.: Initial Conditions: $\text{Particle1-}u[1] = 0.98$, $\text{Particle1-}u[2] = 0.01$ and $\text{Particle1-}u[3] = 0.0$. The particle history is calculated for $t = 400 * \text{pow}(10, 7)$ prior to the simulation. The pictures are taken at $t = 1100 * \text{pow}(10, 7)$.

The electron has an energy of $\gamma = 1.4$. We used the external pulse from above as external field and is therefore not shown here. The colorbar shows the value of $|\vec{E}|^2$. \vec{E} and $c\vec{B}$ are in units of $4\pi\epsilon_0 m_e^2 c^4/e^3 = 1.77 \cdot 10^{20} \text{ V m}^{-1}$, length in units of $e^2/(4\pi\epsilon_0 m_e c^2) = 2.82 \cdot 10^{-15} \text{ m}$ and times in units of $e^2/(4\pi\epsilon_0 m_e c^3) = 9.40 \cdot 10^{-24} \text{ s}$.

Figure 4.23: Ratio of the damping force g^μ and Lorentz force F_L at $\gamma = 1.4$. g^μ was calculated at each time step according to (2.3). Obviously, the damping term g^μ can be neglected. Time is in units of $e^2/(4\pi\epsilon_0 m_e c^3) = 9.40 \cdot 10^{-24} \text{ s}$.



CHAPTER 4. HYBRID FIELD APPROACH

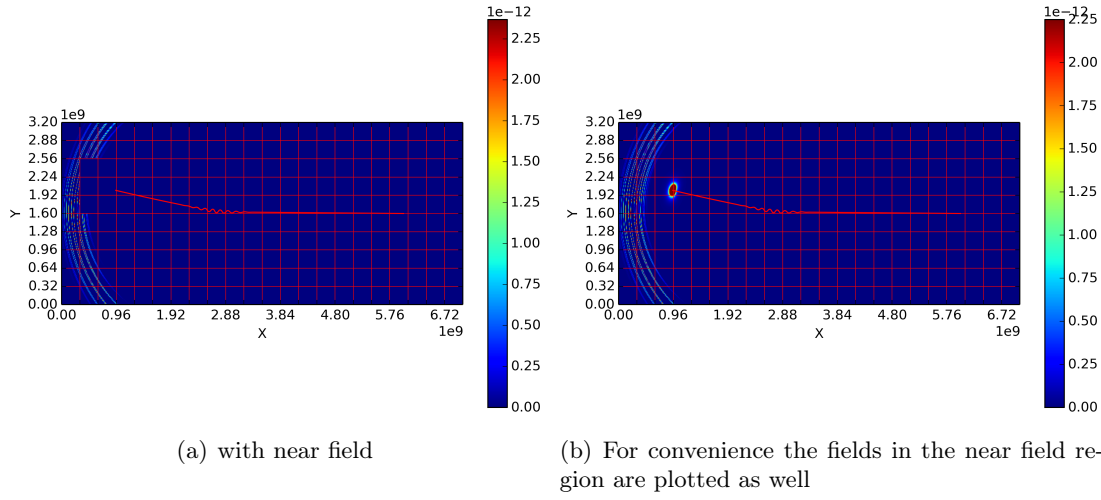


Figure 4.24.: Initial Conditions: `Particle1->u[1] = 1.12`, `Particle1->u[2] = 0.01`
 and `Particle1->u[3] = 0.0`. The particle history is calculated for $t = 400 * \text{pow}(10, 7)$ prior to the simulation. The pictures are taken at $t = 1100 * \text{pow}(10, 7)$.

The electron has an energy of $\gamma = 1.5$. We used the external pulse from above as external field and is therefore not shown here. The colorbar shows the value of $|\vec{E}|^2$. \vec{E} and $c\vec{B}$ are in units of $4\pi\epsilon_0 m_e^2 c^4/e^3 = 1.77 \cdot 10^{20} \text{ V m}^{-1}$, length in units of $e^2/(4\pi\epsilon_0 m_e c^2) = 2.82 \cdot 10^{-15} \text{ m}$ and times in units of $e^2/(4\pi\epsilon_0 m_e c^3) = 9.40 \cdot 10^{-24} \text{ s}$.

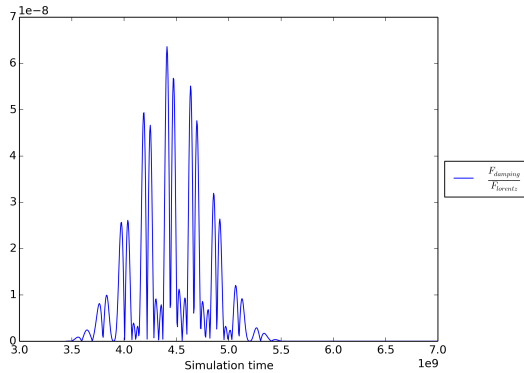


Figure 4.25: Ratio of the damping force g^μ and Lorentz force F_L at $\gamma = 1.5$. g^μ was calculated at each time step according to (2.3). Obviously, the damping term g^μ can be neglected. Time is in units of $e^2/(4\pi\epsilon_0 m_e c^3) = 9.40 \cdot 10^{-24}$ s.

CHAPTER 4. HYBRID FIELD APPROACH

In the next step the electric field components \vec{E} as well as the Poynting vector \vec{S} are 2D Fourier analyzed. The results are shown in figures 4.26 - 4.37

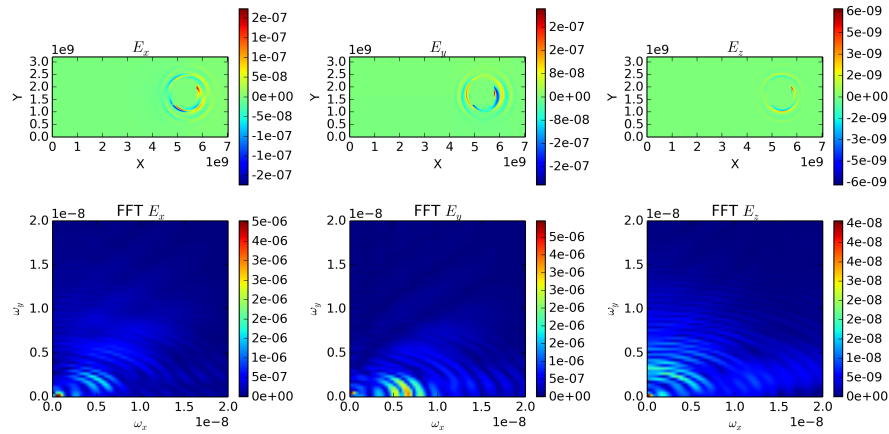


Figure 4.26.: Fourier analysis of the electric field components of \vec{E} at $\gamma = 1.0$. The colorbar shows the value of $|\vec{E}|^2$. \vec{E} and $c\vec{B}$ are in units of $4\pi\epsilon_0 m_e^2 c^4 / e^3 = 1.77 \cdot 10^{20} \text{ V m}^{-1}$, length in units of $e^2 / (4\pi\epsilon_0 m_e c^2) = 2.82 \cdot 10^{-15} \text{ m}$ and times in units of $e^2 / (4\pi\epsilon_0 m_e c^3) = 9.40 \cdot 10^{-24} \text{ s}$.

CHAPTER 4. HYBRID FIELD APPROACH

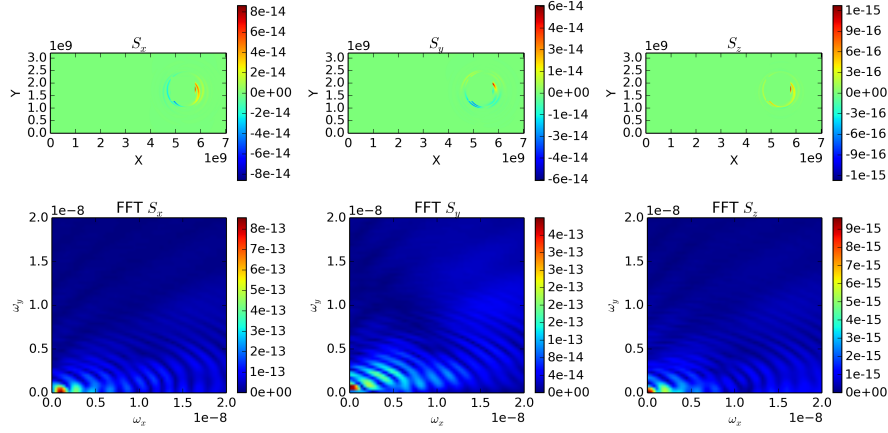


Figure 4.27.: Fourier analysis of the components of the Poynting vector \vec{S} at $\gamma = 1.0$. The colorbar shows the value of $|\vec{E}|^2$. \vec{E} and $c\vec{B}$ are in units of $4\pi\epsilon_0 m_e^2 c^4 / e^3 = 1.77 \cdot 10^{20} \text{ V m}^{-1}$, length in units of $e^2 / (4\pi\epsilon_0 m_e c^2) = 2.82 \cdot 10^{-15} \text{ m}$ and times in units of $e^2 / (4\pi\epsilon_0 m_e c^3) = 9.40 \cdot 10^{-24} \text{ s}$.

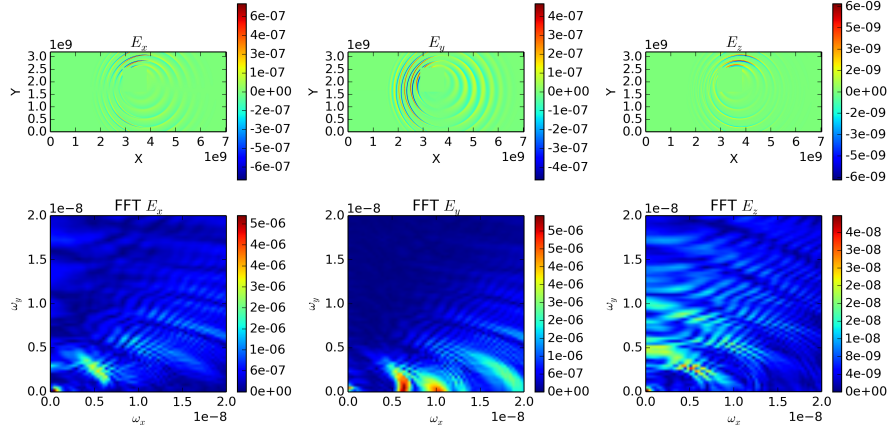


Figure 4.28.: Fourier analysis of the electric field components of \vec{E} at $\gamma = 1.1$. The colorbar shows the value of $|\vec{E}|^2$. \vec{E} and $c\vec{B}$ are in units of $4\pi\epsilon_0 m_e^2 c^4 / e^3 = 1.77 \cdot 10^{20} \text{ V m}^{-1}$, length in units of $e^2 / (4\pi\epsilon_0 m_e c^2) = 2.82 \cdot 10^{-15} \text{ m}$ and times in units of $e^2 / (4\pi\epsilon_0 m_e c^3) = 9.40 \cdot 10^{-24} \text{ s}$.

CHAPTER 4. HYBRID FIELD APPROACH

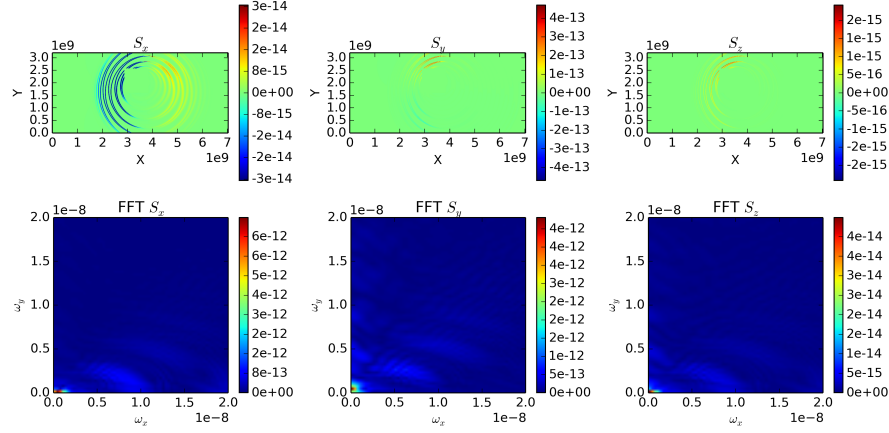


Figure 4.29.: Fourier analysis of the components of the Poynting vector \vec{S} at $\gamma = 1.1$. The colorbar shows the value of $|\vec{E}|^2$. \vec{E} and $c\vec{B}$ are in units of $4\pi\epsilon_0 m_e^2 c^4 / e^3 = 1.77 \cdot 10^{20} \text{ V m}^{-1}$, length in units of $e^2 / (4\pi\epsilon_0 m_e c^2) = 2.82 \cdot 10^{-15} \text{ m}$ and times in units of $e^2 / (4\pi\epsilon_0 m_e c^3) = 9.40 \cdot 10^{-24} \text{ s}$.

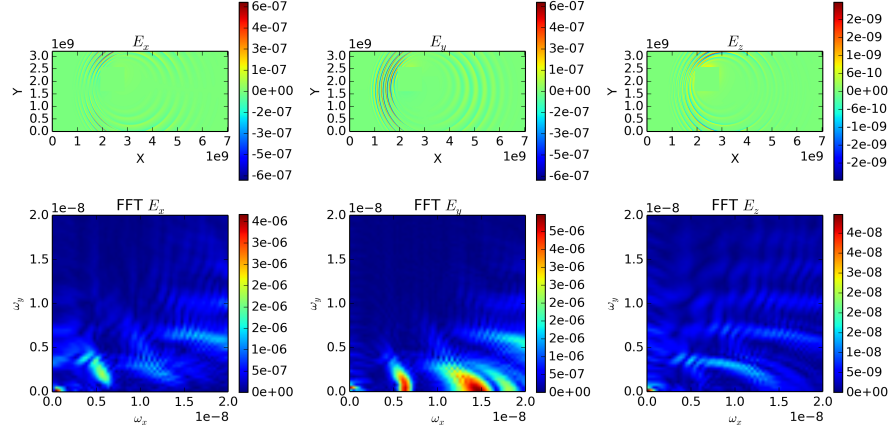


Figure 4.30.: Fourier analysis of the electric field components of \vec{E} at $\gamma = 1.2$. The colorbar shows the value of $|\vec{E}|^2$. \vec{E} and $c\vec{B}$ are in units of $4\pi\epsilon_0 m_e^2 c^4 / e^3 = 1.77 \cdot 10^{20} \text{ V m}^{-1}$, length in units of $e^2 / (4\pi\epsilon_0 m_e c^2) = 2.82 \cdot 10^{-15} \text{ m}$ and times in units of $e^2 / (4\pi\epsilon_0 m_e c^3) = 9.40 \cdot 10^{-24} \text{ s}$.

CHAPTER 4. HYBRID FIELD APPROACH

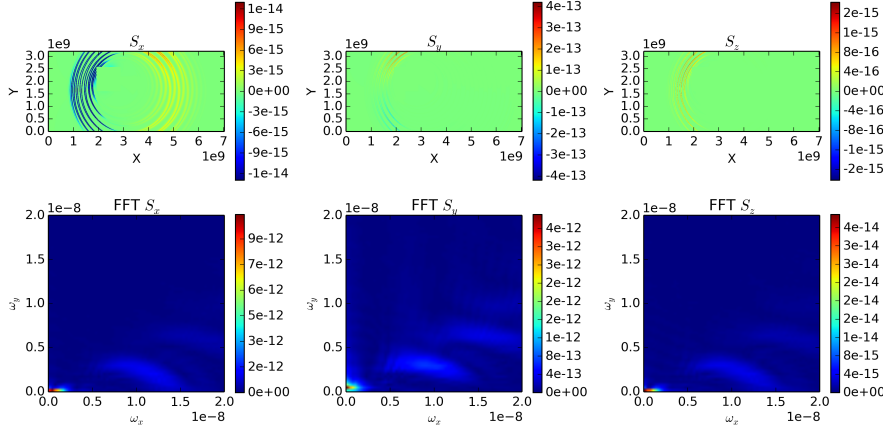


Figure 4.31.: Fourier analysis of the components of the Poynting vector \vec{S} at $\gamma = 1.2$. The colorbar shows the value of $|\vec{E}|^2$. \vec{E} and $c\vec{B}$ are in units of $4\pi\epsilon_0 m_e^2 c^4 / e^3 = 1.77 \cdot 10^{20} \text{ V m}^{-1}$, length in units of $e^2 / (4\pi\epsilon_0 m_e c^2) = 2.82 \cdot 10^{-15} \text{ m}$ and times in units of $e^2 / (4\pi\epsilon_0 m_e c^3) = 9.40 \cdot 10^{-24} \text{ s}$.

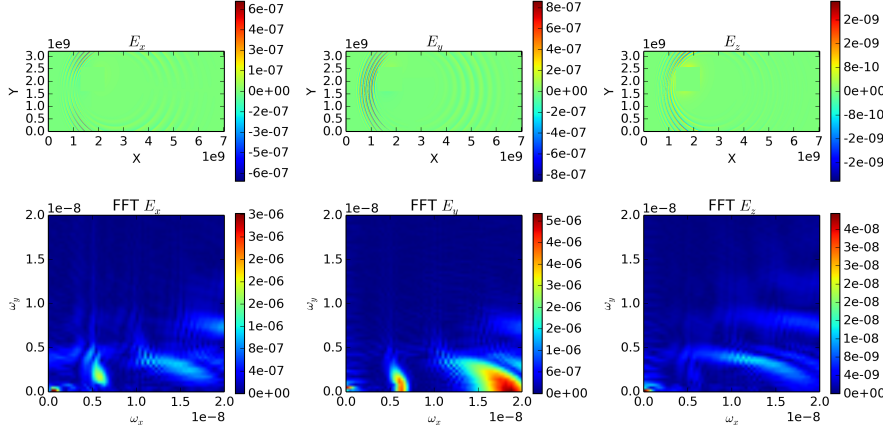


Figure 4.32.: Fourier analysis of the electric field components of \vec{E} at $\gamma = 1.3$. The colorbar shows the value of $|\vec{E}|^2$. \vec{E} and $c\vec{B}$ are in units of $4\pi\epsilon_0 m_e^2 c^4 / e^3 = 1.77 \cdot 10^{20} \text{ V m}^{-1}$, length in units of $e^2 / (4\pi\epsilon_0 m_e c^2) = 2.82 \cdot 10^{-15} \text{ m}$ and times in units of $e^2 / (4\pi\epsilon_0 m_e c^3) = 9.40 \cdot 10^{-24} \text{ s}$.

CHAPTER 4. HYBRID FIELD APPROACH

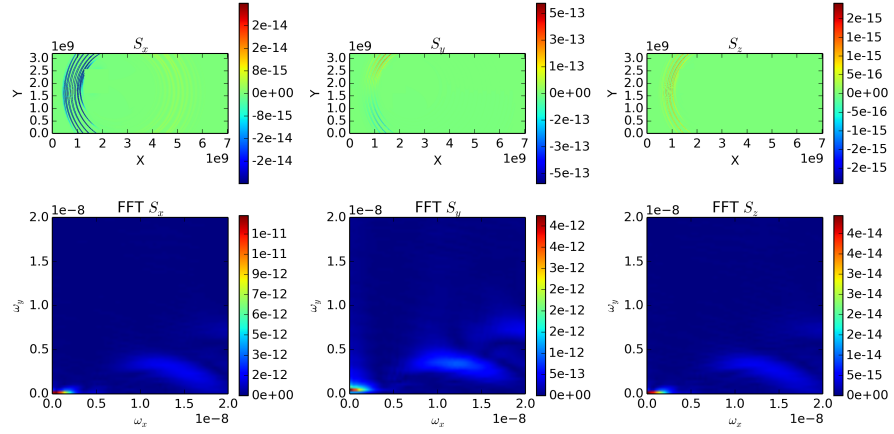


Figure 4.33.: Fourier analysis of the components of the Poynting vector \vec{S} at $\gamma = 1.3$. The colorbar shows the value of $|\vec{E}|^2$. \vec{E} and $c\vec{B}$ are in units of $4\pi\epsilon_0 m_e^2 c^4 / e^3 = 1.77 \cdot 10^{20} \text{ V m}^{-1}$, length in units of $e^2 / (4\pi\epsilon_0 m_e c^2) = 2.82 \cdot 10^{-15} \text{ m}$ and times in units of $e^2 / (4\pi\epsilon_0 m_e c^3) = 9.40 \cdot 10^{-24} \text{ s}$.

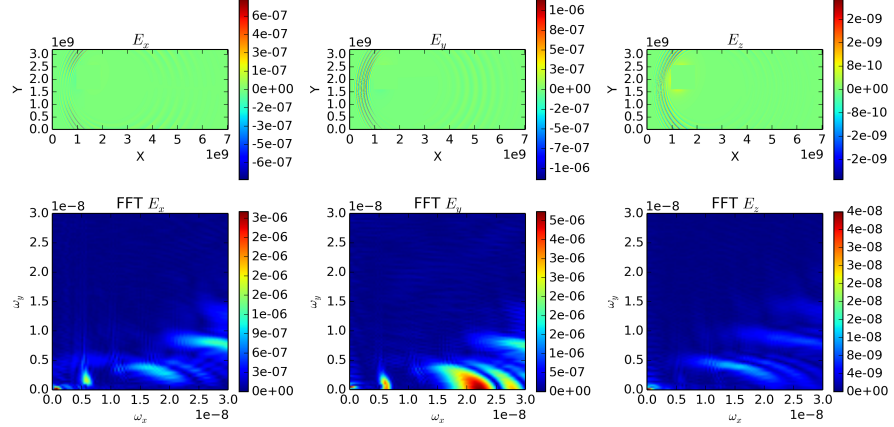


Figure 4.34.: Fourier analysis of the electric field components of \vec{E} at $\gamma = 1.4$. The colorbar shows the value of $|\vec{E}|^2$. \vec{E} and $c\vec{B}$ are in units of $4\pi\epsilon_0 m_e^2 c^4 / e^3 = 1.77 \cdot 10^{20} \text{ V m}^{-1}$, length in units of $e^2 / (4\pi\epsilon_0 m_e c^2) = 2.82 \cdot 10^{-15} \text{ m}$ and times in units of $e^2 / (4\pi\epsilon_0 m_e c^3) = 9.40 \cdot 10^{-24} \text{ s}$.

CHAPTER 4. HYBRID FIELD APPROACH

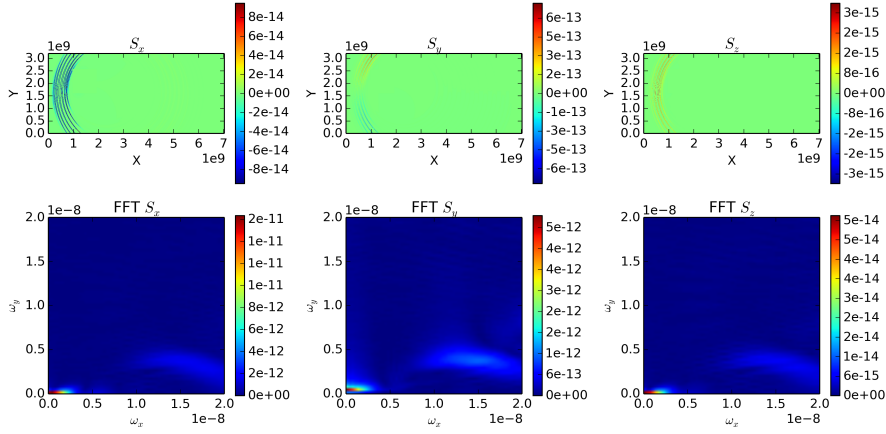


Figure 4.35.: Fourier analysis of the components of the Poynting vector \vec{S} at $\gamma = 1.4$. The colorbar shows the value of $|\vec{E}|^2$. \vec{E} and $c\vec{B}$ are in units of $4\pi\epsilon_0 m_e^2 c^4 / e^3 = 1.77 \cdot 10^{20} \text{ V m}^{-1}$, length in units of $e^2 / (4\pi\epsilon_0 m_e c^2) = 2.82 \cdot 10^{-15} \text{ m}$ and times in units of $e^2 / (4\pi\epsilon_0 m_e c^3) = 9.40 \cdot 10^{-24} \text{ s}$.

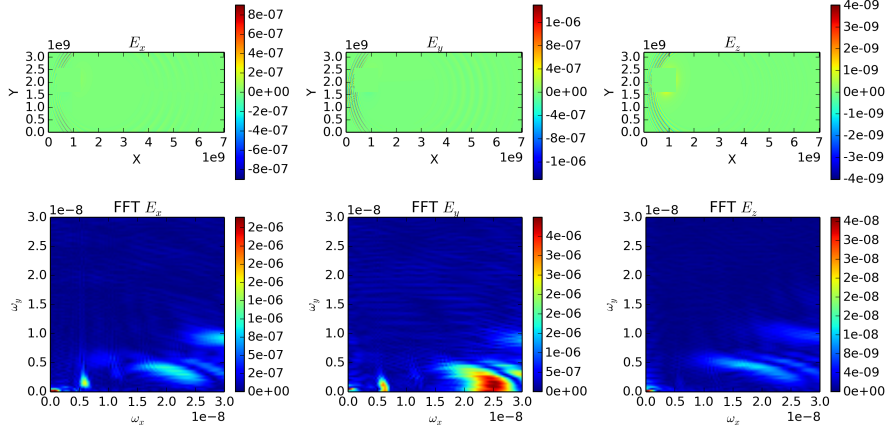


Figure 4.36.: Fourier analysis of the electric field components of \vec{E} at $\gamma = 1.5$. The colorbar shows the value of $|\vec{E}|^2$. \vec{E} and $c\vec{B}$ are in units of $4\pi\epsilon_0 m_e^2 c^4 / e^3 = 1.77 \cdot 10^{20} \text{ V m}^{-1}$, length in units of $e^2 / (4\pi\epsilon_0 m_e c^2) = 2.82 \cdot 10^{-15} \text{ m}$ and times in units of $e^2 / (4\pi\epsilon_0 m_e c^3) = 9.40 \cdot 10^{-24} \text{ s}$.

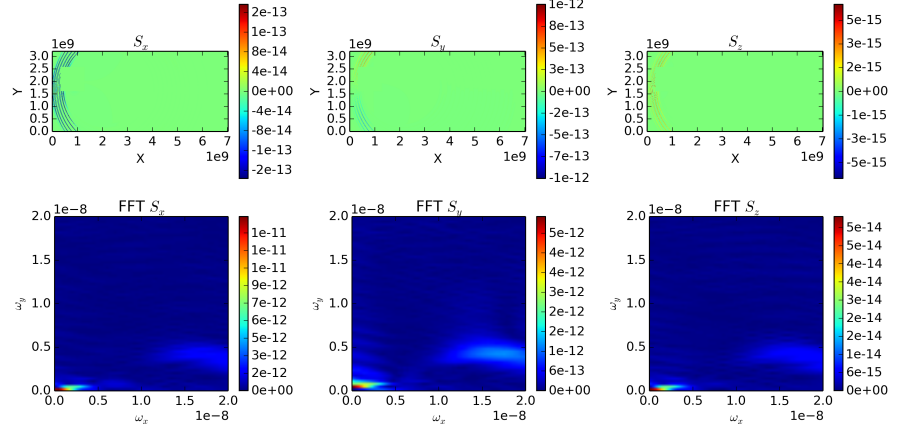


Figure 4.37.: Fourier analysis of the components of the Poynting vector \vec{S} at $\gamma = 1.5$. The colorbar shows the value of $|\vec{E}|^2$. \vec{E} and $c\vec{B}$ are in units of $4\pi\epsilon_0 m_e^2 c^4 / e^3 = 1.77 \cdot 10^{20} \text{ V m}^{-1}$, length in units of $e^2 / (4\pi\epsilon_0 m_e c^2) = 2.82 \cdot 10^{-15} \text{ m}$ and times in units of $e^2 / (4\pi\epsilon_0 m_e c^3) = 9.40 \cdot 10^{-24} \text{ s}$.

5

Uniaxial Perfectly Matched Layer

5.1 Introduction

In this chapter we want to discuss an important topic: Boundary Conditions.

Boundary Conditions apply at the edge of the numerical grid and dictate how the solution is treated, when approaching the edge. The Dirichlet boundary condition, for instance, sets the solution to zero, leading to reflections¹. Periodic boundary conditions extend the grid by setting one edge on top of the opposite one. Solutions leaving the grid to the right enter the simulation area to the left again.

When solving differential equations numerically one always has to think about which boundary conditions apply best for the problem at hand. The most commonly used ones are the two aforementioned ones. Dirichlet boundary conditions apply for physical problems involving fast decaying solutions in space so that truncation does not matter, as long as the numerical grid is large enough. Other problems, like periodic structures, can be simulated with periodic boundary conditions. However, one of the most challenging problems to truncate involve wave equations, like in our case, since their solution only decays slowly². Using periodic, Dirichlet or Neumann boundary conditions will lead to unacceptable artifacts from boundary reflections. One approach is the *absorbing boundary condition* [20]. It turns out that this approach works just fine for the one dimensional case, i.e. waves traveling in only one direction. However, most problems - like ours - include three dimensions. So, we are left where we started. Fortunately in 1994 Berenger came up with a new idea and presented it in his seminal paper [3]. Instead of having an absorbing boundary condition he rather proposed an absorbing boundary layer. The layer is part of the grid and has a specified width. When a wave enters the layer, it is attenuated by the absorption and decays exponentially. Now the problem remains, that the absorbing layer represents an interface where the impedance change, which

¹It's like a rope with a fixed connection to a wall. Since the energy can not be transferred to the wall, all energy is reflected, causing the incident wave to move back.

²Energy conservation requires the energy flux $|S| \propto |E|^2$ to decay inversely proportional to the surface area $\sim r^2$ in three dimensions. Therefore, $|E| \propto \frac{1}{r}$.

in turn causes reflection and transmission. Berenger, however, showed that it's possible to construct a medium which does not reflect any incident wave, independent of angle, polarization and frequency. A so called PML - *Perfectly Matched Layer*. Aside from Berenger's original formulation -the *split field* PML - some equivalent descriptions of PML came up over the years. For one there are the *uniaxial* PML (UPML) which we use in this thesis and dive into more detail below. The most elegant and general description is the *stretched coordinate* PML [7, 17, 21], which is based upon an analytic continuation of Maxwell's equations into complex spatial coordinates. Both the split field PML and the UPML can be derived from this approach.

5.2 Derivation

The most common formulation is the UPML. Following [19, 20] we will present an overview of the most important steps to understand why UPML works and how to implement it.

It will turn out that the medium inside our PML needs to be anisotropic. We will see why later. Being able to describe anisotropic phenomenon we need to incorporate anisotropy into Maxwell Equations. We can do this by making the permittivity ϵ_r and permeability μ_r tensors³. The time harmonic Maxwell's Curl equations then read

$$\begin{aligned}\vec{\nabla} \times \vec{E}(\omega) &= -j\omega\mu_0 [\mu_r] \vec{H}(\omega), \\ \vec{\nabla} \times \vec{H}(\omega) &= \sigma \vec{E}(\omega) + j\omega \vec{D}(\omega),\end{aligned}\tag{5.1}$$

with the relation $\vec{D}(\omega) = \epsilon_0 [\epsilon_r] \vec{E}$ and conductivity σ . As usual, ϵ_0 and ϵ_r are the vacuum and relative permittivity respectively. We start in the frequency domain, because PML is a frequency domain concept and thus it's easier to work with in frequency domain. We will, however, transform back to time domain later in order to get the update equations,

³There are three types of anisotropic media:

$$\text{isotropic: } \begin{bmatrix} a & 0 & 0 \\ 0 & a & 0 \\ 0 & 0 & a \end{bmatrix}, \text{ uniaxial: } \begin{bmatrix} a & 0 & 0 \\ 0 & a & 0 \\ 0 & 0 & b \end{bmatrix}, \text{ biaxial: } \begin{bmatrix} a & 0 & 0 \\ 0 & b & 0 \\ 0 & 0 & c \end{bmatrix}.$$

It is also possible to always choose a coordinate system such that the tensor becomes diagonal.

which we will need to implement. So, (5.1) can be rewritten as

$$\begin{aligned} \begin{pmatrix} 0 & -\frac{\partial}{\partial z} & \frac{\partial}{\partial y} \\ \frac{\partial}{\partial z} & 0 & -\frac{\partial}{\partial x} \\ -\frac{\partial}{\partial y} & \frac{\partial}{\partial x} & 0 \end{pmatrix} \begin{pmatrix} H_x \\ H_y \\ H_z \end{pmatrix} &= j\omega\epsilon_0 \begin{bmatrix} \epsilon_x + \frac{\sigma_x^E}{j\omega} & 0 & 0 \\ 0 & \epsilon_y + \frac{\sigma_y^E}{j\omega} & 0 \\ 0 & 0 & \epsilon_z + \frac{\sigma_z^E}{j\omega} \end{bmatrix} \begin{pmatrix} E_x \\ E_y \\ E_z \end{pmatrix} \quad (5.2) \\ \begin{pmatrix} 0 & -\frac{\partial}{\partial z} & \frac{\partial}{\partial y} \\ \frac{\partial}{\partial z} & 0 & -\frac{\partial}{\partial x} \\ -\frac{\partial}{\partial y} & \frac{\partial}{\partial x} & 0 \end{pmatrix} \begin{pmatrix} E_x \\ E_y \\ E_z \end{pmatrix} &= -j\omega\mu_0 \begin{bmatrix} \mu_x + \frac{\sigma_x^H}{j\omega} & 0 & 0 \\ 0 & \mu_y + \frac{\sigma_y^H}{j\omega} & 0 \\ 0 & 0 & \mu_z + \frac{\sigma_z^H}{j\omega} \end{bmatrix} \begin{pmatrix} H_x \\ H_y \\ H_z \end{pmatrix} \end{aligned}$$

Now we need to talk about reflection and transmission at a surface. In the case of a wave with arbitrary polarization and angle of incidence, as illustrated in Figure 5.1, we can use *Fresnel* equations.⁴ We see that the reflection is a consequence of a change in impedance and also critically angle dependent. It's only possible to match the impedances at one specific angle. However, by introducing anisotropy we can solve this problem. We know that the impedance is given by

$$\eta = \sqrt{\frac{\mu}{\epsilon}}. \quad (5.4)$$

Thus, to keep the impedances matched throughout the entire grid, including the absorbing layer, we need $[\epsilon_r] = [\mu_r]$. This is called an doubly anisotropic media. For convenience let's define

$$[s] := [\epsilon_r] = [\mu_r] = \begin{bmatrix} a & 0 & 0 \\ 0 & b & 0 \\ 0 & 0 & c \end{bmatrix}, \quad (5.5)$$

⁴

$$\begin{aligned} r_{TE} &= \frac{\eta_2 \cos(\theta_1) - \eta_1 \cos(\theta_2)}{\eta_2 \cos(\theta_1) + \eta_1 \cos(\theta_2)}, \\ t_{TE} &= \frac{2\eta_2 \cos(\theta_1)}{\eta_2 \cos(\theta_1) + \eta_1 \cos(\theta_2)}, \\ r_{TM} &= \frac{\eta_2 \cos(\theta_2) - \eta_1 \cos(\theta_1)}{\eta_1 \cos(\theta_1) + \eta_2 \cos(\theta_2)}, \\ t_{TM} &= \frac{2\eta_1 \cos(\theta_1)}{\eta_1 \cos(\theta_1) + \eta_2 \cos(\theta_2)}, \end{aligned} \quad (5.3)$$

where η_i is the impedance in region i with refractive index n_i , θ_1 the angle of incidence and θ_2 the angle of transmission.

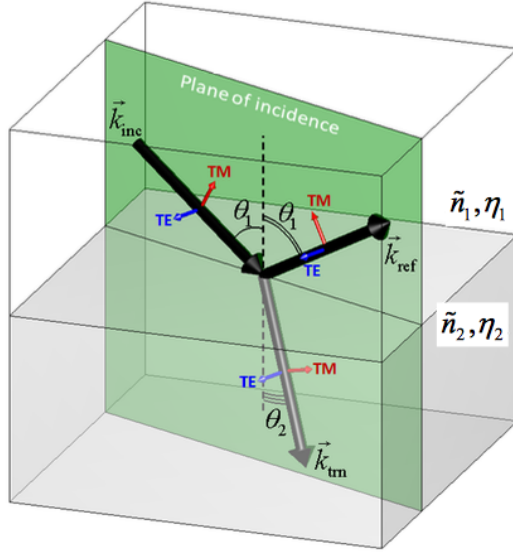


Figure 5.1.: Wave with wavevector \vec{k} , arbitrary polarization and angle of incidence θ at a surface with impedance η_i and refractive index n_i [19].

with a, b, c to be determined. Considering anisotropy the Fresnel Equations change. For example for an incident wave traveling along z-axis, the Fresnel Equations read

$$\begin{aligned} r_{TE} &= \frac{\sqrt{a} \cos(\theta_1) - \sqrt{b} \cos(\theta_2)}{\sqrt{a} \cos(\theta_1) + \sqrt{b} \cos(\theta_2)}, \\ t_{TE} &= \frac{\sqrt{a} \cos(\theta_1)}{\sqrt{a} \cos(\theta_1) + \sqrt{b} \cos(\theta_2)}, \\ r_{TM} &= \frac{-\sqrt{a} \cos(\theta_1) + \sqrt{b} \cos(\theta_2)}{\sqrt{a} \cos(\theta_1) + \sqrt{b} \cos(\theta_2)}, \\ t_{TM} &= \frac{\sqrt{a} \cos(\theta_1)}{\sqrt{b} \cos(\theta_1) + \sqrt{a} \cos(\theta_2)}, \end{aligned} \quad (5.6)$$

where θ_1 the angle of incidence and θ_2 the angle of transmission. These two are connected via Snell's Law

$$\sin(\theta_1) = \sqrt{bc} \sin \theta_2. \quad (5.7)$$

We now need to find conditions for a, b, c to make the Fresnel equations (5.6) independent of angle and simultaneously let the reflection parameter vanish.

If we choose $\sqrt{bc} = 1$ Snell's Law simplifies to $\theta_1 = \theta_2$. Thus the reflection parameters reduce to

$$\begin{aligned} r_{TE} &= \frac{\sqrt{a} - \sqrt{b}}{\sqrt{a} + \sqrt{b}}, \\ r_{TM} &= \frac{-\sqrt{a} + \sqrt{b}}{\sqrt{a} + \sqrt{b}}. \end{aligned} \quad (5.8)$$

With this choice we made the reflection independent of angle! Furthermore, if we require $r_{TE} \stackrel{!}{=} 0$ and $r_{TM} \stackrel{!}{=} 0$ we get $a \stackrel{!}{=} b$. To sum it up, a, b, c need to fulfill

$$a = b = \frac{1}{c}. \quad (5.9)$$

Therefore, our tensor $[s_z]$ needs to look like this

$$[s_z] = \begin{bmatrix} s_z & 0 & 0 \\ 0 & s_z & 0 \\ 0 & 0 & \frac{1}{s_z} \end{bmatrix}. \quad (5.10)$$

Recall that this is an uniaxial tensor. This is the reason why this approach is called Uniaxial Perfectly Matched Layer.

Analogously one gets

$$[s_y] = \begin{bmatrix} s_y & 0 & 0 \\ 0 & \frac{1}{s_z} & 0 \\ 0 & 0 & s_y \end{bmatrix} \text{ and } [s_x] = \begin{bmatrix} \frac{1}{s_z} & 0 & 0 \\ 0 & s_x & 0 \\ 0 & 0 & s_x \end{bmatrix}, \quad (5.11)$$

for waves traveling in y and x direction respectively. These can be combined in a single tensor [20]

$$[s] := [s_x] [s_y] [s_z] = \begin{bmatrix} \frac{s_y s_z}{s_x} & 0 & 0 \\ 0 & \frac{s_x s_z}{s_y} & 0 \\ 0 & 0 & \frac{s_x s_y}{s_z} \end{bmatrix}, \quad (5.12)$$

where

$$\begin{aligned} s_x(x) &= \kappa_x + \frac{\sigma'_x(x)}{j\omega_0\epsilon_0} \\ s_y(y) &= \kappa_y + \frac{\sigma'_y(y)}{j\omega_0\epsilon_0} \\ s_z(z) &= \kappa_z + \frac{\sigma'_z(z)}{j\omega_0\epsilon_0}. \end{aligned} \quad (5.13)$$

We will specify σ' and κ later. Having this, the Maxwell Equations (5.1) now read

$$\begin{aligned} \vec{\nabla} \times \vec{E}(\omega) &= -j\omega\mu_0 [\mu_r] [s] \vec{H}(\omega), \\ \vec{\nabla} \times \vec{H}(\omega) &= \sigma \vec{E}(\omega) + j\omega [s] \vec{D}(\omega). \end{aligned} \quad (5.14)$$

Before we start to derive the update equations, we normalize our electric field as follows

$$\begin{aligned} \vec{\tilde{E}} &= \sqrt{\frac{\epsilon_0}{\mu_0}} \vec{E} = \frac{1}{\eta_0} \vec{E} \\ \vec{\tilde{D}} &= \frac{1}{\sqrt{\mu_0\epsilon_0}} \vec{D} = c_0 \vec{D}, \end{aligned} \quad (5.15)$$

which yields

$$\begin{aligned} \vec{\nabla} \times \vec{\tilde{E}}(\omega) &= -j\omega\mu_0 \frac{[\mu_r]}{c_0} [s] \vec{\tilde{H}}(\omega), \\ \vec{\nabla} \times \vec{\tilde{H}}(\omega) &= \eta_0 \sigma \vec{\tilde{E}}(\omega) + \frac{j\omega}{c_0} [s] \vec{\tilde{D}}(\omega). \end{aligned} \quad (5.16)$$

5.3 Update Equations

We now want to derive the update equations from (5.16). For simplicity we focus on Ampere's Law and consider the case, where the interior of our simulation area has no loss ($\sigma = 0$). Only the PML will have loss ($\sigma' \neq 0$). Ampere's Law rewritten in matrix form then simplifies to

$$\begin{pmatrix} \frac{\partial H_z}{\partial y} - \frac{\partial H_y}{\partial z} \\ \frac{\partial H_x}{\partial z} - \frac{\partial H_z}{\partial x} \\ \frac{\partial H_y}{\partial x} - \frac{\partial H_x}{\partial y} \end{pmatrix} = j\omega \begin{bmatrix} s_x & 0 & 0 \\ 0 & s_y & 0 \\ 0 & 0 & s_z \end{bmatrix} \begin{pmatrix} \tilde{D}_x \\ \tilde{D}_y \\ \tilde{D}_z \end{pmatrix}. \quad (5.17)$$

Substituting (5.13) into (5.17) and using the fourier identity

$$\mathcal{F} \left\{ \frac{\partial^n}{\partial t^n} g(t) \right\} = (j\omega)^n G(\omega), \quad (5.18)$$

where g is a piecewise \mathcal{C}^1 function and $g \in \mathcal{L}^1(\mathbb{R})$ yields the following system of time domain equations

$$\begin{pmatrix} \frac{\partial H_z}{\partial y} - \frac{\partial H_y}{\partial z} \\ \frac{\partial H_x}{\partial z} - \frac{\partial H_z}{\partial x} \\ \frac{\partial H_y}{\partial x} - \frac{\partial H_x}{\partial y} \end{pmatrix} = \frac{\partial}{\partial t} \begin{bmatrix} \kappa_x & 0 & 0 \\ 0 & \kappa_y & 0 \\ 0 & 0 & \kappa_z \end{bmatrix} \begin{pmatrix} \tilde{D}_x \\ \tilde{D}_y \\ \tilde{D}_z \end{pmatrix} + \frac{1}{\epsilon_0} \begin{bmatrix} \sigma'_x & 0 & 0 \\ 0 & \sigma'_y & 0 \\ 0 & 0 & \sigma'_z \end{bmatrix} \begin{pmatrix} \tilde{D}_x \\ \tilde{D}_y \\ \tilde{D}_z \end{pmatrix}. \quad (5.19)$$

The system (5.19) can be discretized with Yee-Scheme, as explained in Section 4.1 and using central differences. Because it's quite longish and a lot's of Algebra we ommitt it here and refer to literature instead (see [19, 20]). For instance, the D_x update is given by

$$D_x|_{(i+\frac{1}{2}, j, k)}^{n+1} = \left(\frac{2\epsilon_0\kappa_y - \sigma'_y h}{2\epsilon_0\kappa_y + \sigma'_y h} \right) D_x|_{i+\frac{1}{2}, j, k}^n + \left(\frac{2\epsilon_0 h}{2\epsilon_0\kappa_y + \sigma'_y h} \right) \left(\frac{H_z|_{(i+\frac{1}{2}, j+\frac{1}{2}, k)}^{n+\frac{1}{2}} - H_z|_{(i+\frac{1}{2}, j-\frac{1}{2}, k)}^{n+\frac{1}{2}}}{\Delta y} - \frac{H_y|_{(i+\frac{1}{2}, j, k+\frac{1}{2})}^{n+\frac{1}{2}} - H_y|_{(i+\frac{1}{2}, j, k-\frac{1}{2})}^{n+\frac{1}{2}}}{\Delta z} \right). \quad (5.20)$$

From $\vec{D}(\omega) = \epsilon_0 [\epsilon_r] \vec{E}$ the update equation for \vec{E} can be derived

$$E_x|_{(i+\frac{1}{2}, j, k)}^{n+1} = \left(\frac{2\epsilon_0\kappa_z - \sigma'_z h}{2\epsilon_0\kappa_z + \sigma'_z h} \right) E_x|_{i+\frac{1}{2}, j, k}^n + \left(\frac{1}{(2\epsilon_0\kappa_z + \sigma'_z h)\epsilon} \right) \left((2\epsilon_0\kappa_x + \sigma'_x h) D_x|_{i+\frac{1}{2}, j, k}^{n+1} - (2\epsilon_0\kappa_x - \sigma'_x h) D_x|_{i+\frac{1}{2}, j, k}^n \right). \quad (5.21)$$

As we can see, the update equation for $E_x|_{(i+\frac{1}{2}, j, k)}^{n+1}$ contains the term $D_x|_{i+\frac{1}{2}, j, k}^{n+1}$. Consequently the update process of E_x requires an update of D_x first. So, we first calculate D_x for the next time step and use this result to update E_x . The same procedure applies

for the update equations of B_x and H_x

$$\begin{aligned} \textcolor{blue}{B_x}|_{(i,j+\frac{1}{2},k+\frac{1}{2})}^{n+\frac{3}{2}} &= \left(\frac{2\epsilon_0\kappa_y - \sigma'_y h}{2\epsilon_0\kappa_y + \sigma'_y h} \right) B_x|_{(i,j+\frac{1}{2},k+\frac{1}{2})}^{n+\frac{1}{2}} + \left(\frac{2\epsilon_0 h}{2\epsilon_0\kappa_y + \sigma'_y h} \right) \\ &\quad \left(\frac{E_z|_{(i,j+1,k+\frac{1}{2})}^{n+1} - E_z|_{(i,j,k+\frac{1}{2})}^{n+1}}{\Delta y} - \frac{E_y|_{(i,j+\frac{1}{2},k+1)}^{n+1} - E_y|_{(i,j+\frac{1}{2},k)}^{n+1}}{\Delta z} \right), \end{aligned} \quad (5.22)$$

$$\begin{aligned} H_x|_{(i,j+\frac{1}{2},k+\frac{1}{2})}^{n+\frac{3}{2}} &= \left(\frac{2\epsilon_0\kappa_z - \sigma'_z h}{2\epsilon_0\kappa_z + \sigma'_z h} \right) H_x|_{(i,j+\frac{1}{2},k+\frac{1}{2})}^{n+\frac{1}{2}} + \left(\frac{1}{(2\epsilon_0\kappa_z + \sigma'_z h)\mu} \right) \\ &\quad \left((2\epsilon_0\kappa_x + \sigma'_x h) \textcolor{blue}{B_x}|_{(i,j+\frac{1}{2},k+\frac{1}{2})}^{n+\frac{3}{2}} - (2\epsilon_0\kappa_x - \sigma'_x h) B_x|_{(i,j+\frac{1}{2},k+\frac{1}{2})}^{n+\frac{1}{2}} \right). \end{aligned} \quad (5.23)$$

Notice that if we turn off the PML, i.e. $\sigma' = 0$ and $\kappa = 1$ the prefactors simplify drastically. Plugging in (5.20) into (5.21) and also (5.22) into (5.23) result in the discretized Maxwell Equations, as we derived them in (4.1). Of course, the update equations of the other field components can be derived analogously.

5.4 Implementation of UPML in FDTD

Finally, we want to show, how to implement UPML into an existing FDTD simulation. Since all the prefactors are constants, it's advisable to calculate them beforehand. Here is a snippet of the code

```
Grid->upml1E[j] = (2 * kappa - sigma * dt) / (2 * kappa + sigma * dt);
Grid->upml2E[j] = (2 * dt) / (2 * kappa + sigma * dt);
Grid->upml3E[k] = (2 * kappa - sigma * dt) / (2 * kappa + sigma * dt);
Grid->upml4E[k] = 1.0 / (2 * kappa + sigma * dt);
Grid->upml5E[i] = (2 * kappa + sigma * dt);
Grid->upml6E[i] = (2 * kappa - sigma * dt);
```

The same applies for the H components.

From a theoretical point of view, a reflectionless PML is possible. In practice, however, numerical artifacts arise, due to finite spatial sampling [20]. The change from σ in the interior to σ' in the PML is effectively a local discontinuity and thus causes reflections. For best performance, Berenger proposed that the PML losses σ' shall gradually rise

from zero at $x = 0$ to σ_{max} at $x = d$, where d is the PML layer width [3]

$$\begin{aligned}\sigma_x(x) &= \left(\frac{x}{d}\right)^m \sigma_{x,max} \\ \kappa_x(x) &= 1 + (\kappa_{x,max} - 1) \left(\frac{x}{d}\right)^m.\end{aligned}\quad (5.24)$$

m defines the grading and is typically $3 \leq m \leq 4$ in FDTD simulations. We chose $m = 3.5$. Through a lot of testing and experimenting, σ_{max} was found to be [20]

$$\sigma_x^{opt} = \frac{0.8(m+1)}{\eta\Delta x}, \quad (5.25)$$

where $\eta = \sqrt{\frac{\mu}{\epsilon}}$. This of course also applies for the other components of σ .

Figure 5.2 shows how a simulation with UPML looks like

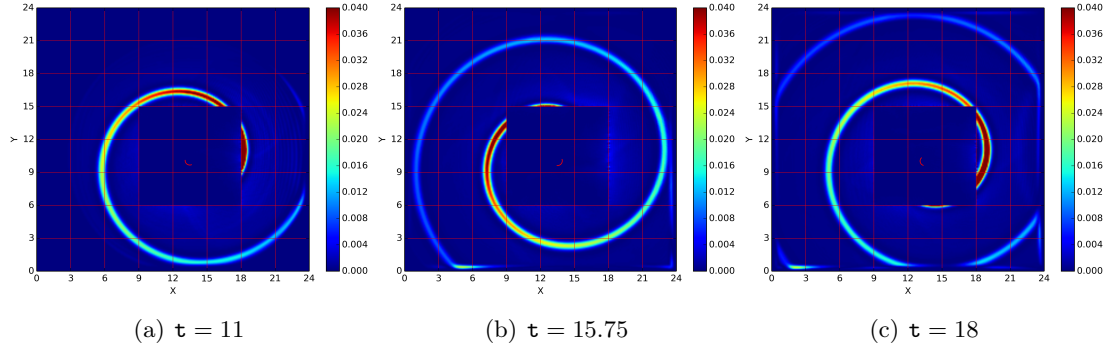


Figure 5.2.: Simulation using UPML.

The electron has an energy of $\gamma = 1.2$. We used a constant $B_z = 1$ as external field. The colorbar shows the value of $|E|^2$. \vec{E} and $c\vec{B}$ are in units of $4\pi\epsilon_0 m_e^2 c^4 / e^3 = 1.77 \cdot 10^{20} \text{ V m}^{-1}$, length in units of $e^2 / (4\pi\epsilon_0 m_e c^2) = 2.82 \cdot 10^{-15} \text{ m}$ and times in units of $e^2 / (4\pi\epsilon_0 m_e c^3) = 9.40 \cdot 10^{-24} \text{ s}$

Part III.

Summary

Part IV.

Appendix

A

Gauge Transformations

In this chapter we want to show, that the gauge fields leave both the electric and magnetic fields and the corresponding potential equations invariant.

A.1 Invariance of Fields

We want to show that $\vec{E}' = \vec{E}$ and $\vec{B}' = \vec{B}$.

$$\begin{aligned}\vec{E}' &= -\vec{\nabla}\varphi' - \frac{\partial\vec{A}'}{\partial t} \\ &= -\vec{\nabla}\left(\varphi - \frac{\partial\psi}{\partial t}\right) - \frac{\partial}{\partial t}\left(\vec{A} + \vec{\nabla}\psi\right) \\ &= -\vec{\nabla}\varphi + \vec{\nabla}\left(\frac{\partial\psi}{\partial t}\right) - \frac{\partial\vec{A}}{\partial t} - \frac{\partial}{\partial t}(\vec{\nabla}\psi) \\ &= \vec{E}\end{aligned}$$

and

$$\begin{aligned}\vec{B}' &= \vec{\nabla} \times \vec{A}' \\ &= \vec{\nabla} \times \left(\vec{A} + \vec{\nabla}\psi\right) \\ &= \vec{\nabla} \times \vec{A} + \vec{\nabla} \times (\vec{\nabla}\psi) \\ &= \vec{B}.\end{aligned}$$

A.2 Invariance of Potential Equations

Now we want to show the invariance of the potential equations. Therefore, consider

$$\begin{aligned}
 -\Delta\varphi' - \vec{\nabla} \left(\frac{\partial \vec{A}'}{\partial t} \right) &= \frac{\rho}{\epsilon_0} \\
 \iff -\Delta \left(\varphi - \frac{\partial \psi}{\partial t} \right) - \vec{\nabla} \left[\frac{\partial}{\partial t} (\vec{A} + \vec{\nabla}\psi) \right] &= \frac{\rho}{\epsilon_0} \\
 \iff -\Delta\varphi + \Delta \left(\frac{\partial \psi}{\partial t} \right) - \vec{\nabla} \left(\frac{\partial \vec{A}}{\partial t} \right) - \vec{\nabla} \left[\frac{\partial}{\partial t} (\vec{\nabla}\psi) \right] &= \frac{\rho}{\epsilon_0} \\
 \iff -\Delta\varphi - \vec{\nabla} \left(\frac{\partial \vec{A}}{\partial t} \right) &= \frac{\rho}{\epsilon_0}
 \end{aligned}$$

and

$$\begin{aligned}
 \square \vec{A}' - \vec{\nabla} \left(\vec{\nabla} \vec{A}' + \frac{1}{c^2} \frac{\partial \varphi'}{\partial t} \right) &= -\mu_0 \vec{j} \\
 \iff \hat{\square} (\vec{A} + \vec{\nabla}\psi) - \vec{\nabla} \left[\vec{\nabla} (\vec{A} + \vec{\nabla}\psi) + \frac{1}{c^2} \frac{\partial}{\partial t} \left(\varphi - \frac{\partial \psi}{\partial t} \right) \right] &= -\mu_0 \vec{j} \\
 \iff \hat{\square} \vec{A} + \square (\vec{\nabla}\psi) - \vec{\nabla} \left[\vec{\nabla} \vec{A} + \Delta\psi + \frac{1}{c^2} \frac{\partial \varphi}{\partial t} - \frac{1}{c^2} \frac{\partial^2 \psi}{\partial t^2} \right] &= -\mu_0 \vec{j} \\
 \iff \hat{\square} \vec{A} + \square (\vec{\nabla}\psi) - \vec{\nabla} \left[\vec{\nabla} \vec{A} + \square\psi + \frac{1}{c^2} \frac{\partial \varphi}{\partial t} \right] &= -\mu_0 \vec{j} \\
 \iff \hat{\square} \vec{A} - \vec{\nabla} \left(\vec{\nabla} \vec{A} + \frac{1}{c^2} \frac{\partial \varphi}{\partial t} \right) &= -\mu_0 \vec{j}
 \end{aligned}$$

B

Retarded Potential Equations Fulfill Laurentz Gauge

We show that the retarded potential equations

$$\begin{aligned}\varphi(\vec{r}, t) &= \frac{1}{4\pi\epsilon_0} \int_V \frac{\rho(\vec{r}', t_{ret})}{|\vec{r} - \vec{r}'|} d\vec{r}', \\ \vec{A}(\vec{r}, t) &= \frac{\mu_0}{4\pi} \int_V \frac{\vec{j}(\vec{r}', t_{ret})}{|\vec{r} - \vec{r}'|} d\vec{r}'\end{aligned}$$

with $t_{ret} := t - \frac{|\vec{r} - \vec{r}'|}{c}$ fulfill the Laurentz Gauge

$$\vec{\nabla} \vec{A} + \frac{1}{c^2} \frac{\partial \varphi}{\partial t} = 0.$$

Plugging in yields

$$\begin{aligned}\vec{\nabla} \vec{A} + \frac{1}{c^2} \frac{\partial \varphi}{\partial t} &= \frac{\mu_0}{4\pi} \int_V \vec{\nabla}_{\vec{r}} \frac{\vec{j}(\vec{r}', t_{ret})}{|\vec{r} - \vec{r}'|} d\vec{r}' + \frac{1}{c^2} \frac{1}{4\pi\epsilon_0} \int_V \frac{\partial}{\partial t} \frac{\rho(\vec{r}', t_{ret})}{|\vec{r} - \vec{r}'|} d\vec{r}' \\ &= \frac{\mu_0}{4\pi} \int_V \vec{\nabla}_{\vec{r}} \frac{\vec{j}(\vec{r}', t_{ret})}{|\vec{r} - \vec{r}'|} \frac{\partial}{\partial t} \frac{\rho(\vec{r}', t_{ret})}{|\vec{r} - \vec{r}'|} d\vec{r}',\end{aligned}$$

where we used $c^2 = \frac{1}{\mu_0\epsilon_0}$. Now consider the first term in the integrand

$$\begin{aligned}\vec{\nabla}_{\vec{r}} \frac{\vec{j}(\vec{r}', t_{ret})}{|\vec{r} - \vec{r}'|} &= \vec{j}(\vec{r}', t_{ret}) \vec{\nabla}_{\vec{r}} \left(\frac{1}{|\vec{r} - \vec{r}'|} \right) + \frac{1}{|\vec{r} - \vec{r}'|} \partial_{t_{ret}} \vec{j}(\vec{r}', t_{ret}) \vec{\nabla}_{\vec{r}} t_{ret} \\ &= -\vec{j}(\vec{r}', t_{ret}) \frac{\vec{r} - \vec{r}'}{|\vec{r} - \vec{r}'|^3} - \frac{1}{c} \frac{\vec{r} - \vec{r}'}{|\vec{r} - \vec{r}'|^2} \partial_{t_{ret}} \vec{j}(\vec{r}', t_{ret})\end{aligned}$$

On the other hand we also have

$$\begin{aligned}\vec{\nabla}_{\vec{r}'} \frac{\vec{j}(\vec{r}', t_{ret})}{|\vec{r} - \vec{r}'|} &= \vec{j}(\vec{r}', t_{ret}) \vec{\nabla}_{\vec{r}'} \left(\frac{1}{|\vec{r} - \vec{r}'|} \right) + \frac{1}{|\vec{r} - \vec{r}'|} \left(\vec{\nabla}_{\vec{r}'} \vec{j}(\vec{r}', t_{ret}) \Big|_{t_{ret}} + \partial_{t_{ret}} \vec{j}(\vec{r}', t_{ret}) \vec{\nabla}_{\vec{r}'} t_{ret} \right) \\ &= \vec{j}(\vec{r}', t_{ret}) \frac{\vec{r} - \vec{r}'}{|\vec{r} - \vec{r}'|^3} + \frac{1}{|\vec{r} - \vec{r}'|} \left(\vec{\nabla}_{\vec{r}'} \vec{j}(\vec{r}', t_{ret}) \Big|_{t_{ret}} + \frac{1}{c} \frac{\vec{r} - \vec{r}'}{|\vec{r} - \vec{r}'|} \partial_{t_{ret}} \vec{j}(\vec{r}', t_{ret}) \right),\end{aligned}$$

APPENDIX B. RETARDED POTENTIAL EQUATIONS FULFILL LAURENTZ GAUGE

which means that we can write

$$\vec{\nabla}_{\vec{r}} \frac{\vec{j}(\vec{r}', t_{ret})}{|\vec{r} - \vec{r}'|} + \vec{\nabla}_{\vec{r}'} \frac{\vec{j}(\vec{r}', t_{ret})}{|\vec{r} - \vec{r}'|} = \frac{\vec{\nabla}_{\vec{r}'} \vec{j}(\vec{r}', t_{ret})|_{t_{ret}}}{|\vec{r} - \vec{r}'|}.$$

Plugging in this into (B.1) yields

$$\vec{\nabla} \vec{A} + \frac{1}{c^2} \frac{\partial \varphi}{\partial t} = \frac{\mu_0}{4\pi} \int_V -\vec{\nabla}_{\vec{r}'} \underbrace{\frac{\vec{j}(\vec{r}', t_{ret})}{|\vec{r} - \vec{r}'|}}_{=0 \text{ due to continuity equation}} + \underbrace{\frac{\vec{\nabla}_{\vec{r}'} \vec{j}(\vec{r}', t_{ret})|_{t_{ret}}}{|\vec{r} - \vec{r}'|}}_{=0 \text{ due to continuity equation}} + \frac{\partial}{\partial t} \frac{\rho(\vec{r}', t_{ret})}{|\vec{r} - \vec{r}'|} d\vec{r}'.$$

For the remaining first term we use *Stokes Law*

$$\vec{\nabla} \vec{A} + \frac{1}{c^2} \frac{\partial \varphi}{\partial t} = -\frac{\mu_0}{4\pi} \int_V \vec{\nabla}_{\vec{r}'} \frac{\vec{j}(\vec{r}', t_{ret})}{|\vec{r} - \vec{r}'|} d\vec{r}' = -\frac{\mu_0}{4\pi} \oint_{\partial V} \frac{\vec{j}(\vec{r}', t_{ret})}{|\vec{r} - \vec{r}'|} d\vec{\sigma} = 0,$$

because the current density vanishes at infinity. That's what we wanted to show.

C

Softwarestack and Documentation

D

Normalization

In this chapter we show how we can make the basic equations from Section 2.1 dimensionless. Even though it's not necessary, it's always advisable in numerics to have a dimensionless systems for reasons of simplicity and clarity. In addition to the transformation equations we will also present the dimensionless Lorentz-Newton equation (2.1), the damping term, i.e. Landau-Lifschitz equation (2.3) and of course the Liénard-Wiechart equations (1.32).

To make the physical entities dimensionless we introduce a characteristic frequency ω . Dimensionless parameters are denoted with a tilde.

With the following transformations

$$\begin{aligned}
 t &= \frac{1}{\omega} \tilde{t}, \\
 \vec{r} &= \frac{c}{\omega} \tilde{\vec{r}}, \\
 R &= \frac{c}{\omega} \tilde{R}, \\
 d\tau &= \frac{1}{\omega} d\tilde{s}, \\
 F^{\mu\nu} &= \frac{\omega m_e}{q} \tilde{F}^{\mu\nu}, \\
 F^{\mu\nu}_{\text{ext}} &= \frac{\omega m_e}{e} \tilde{F}^{\mu\nu}_{\text{ext}}, \\
 F^{\mu\nu}_{\text{lw}} &= \frac{q}{4\pi\epsilon_0} \frac{\omega^2}{c^3} \tilde{F}^{\mu\nu}_{\text{lw}}, \\
 F^{\mu\nu} &= F^{\mu\nu}_{\text{ext}} + \frac{q^2}{4\pi\epsilon_0} \frac{\omega^2}{c^3} \tilde{F}^{\mu\nu}_{\text{lw}}
 \end{aligned} \tag{D.1}$$

the aforementioned equations become dimensionless, where $F^{\mu\nu}_{\text{ext}}$ denotes the external fields, $F^{\mu\nu}_{\text{lw}}$ the Liénard-Wiechart fields and $F^{\mu\nu}$ the total fields. If we define the

APPENDIX D. NORMALIZATION

characteristic frequency ω such, that

$$\begin{aligned} \frac{q^2}{4\pi\epsilon_0} \frac{\omega^2}{c^3} &\stackrel{!}{=} 1 \\ \implies \omega &= 4\pi\epsilon_0 \frac{m_e c^3}{q^2}, \end{aligned} \tag{D.2}$$

both the external and the Liénard-Wiechert fields have the same units

$$\frac{\omega m_e}{q} = 4\pi\epsilon_0 \frac{m_e^2 c^3}{q^3}. \tag{D.3}$$

In the following we present the basic equations from Section 2.1 in dimensionless form:
The dimensionless Lorentz-Newton equation (2.1) reads

$$\frac{du^\mu}{d\tilde{s}} = \left(\tilde{F}^{\mu\nu}_{\text{lw}}(x^\mu) + \tilde{F}^{\mu\nu}_{\text{ext}}(x^\mu) \right) u^\nu + \tilde{g}^\mu. \tag{D.4}$$

The Landau-Lifschitz equation (2.3) becomes

$$\tilde{g}^\mu = \frac{2}{3} \left(\frac{\partial \tilde{F}^{\mu\nu}}{\partial \tilde{x}^\xi} u^\nu u^\xi - \tilde{F}^{\mu\xi} \tilde{F}_{\nu\xi} u^\nu + (\tilde{F}_{\nu\xi} u^\xi)(\tilde{F}^{\nu\pi} u_\pi) u^\mu \right), \tag{D.5}$$

and finally the Liénard-Wiechart equations (1.32)

$$\begin{aligned} \vec{E}(\vec{r}, \tilde{t}) &= \left(\frac{\vec{n}(\vec{r}, \tilde{t}') - \vec{\beta}(\tilde{t})}{\gamma^2 (1 - \vec{\beta}(\tilde{t}) \cdot \vec{n}(\vec{r}, \tilde{t}'))^3 \tilde{R}^2(\vec{r}, \tilde{t}')} \right. \\ &\quad \left. + \frac{\vec{n}(\vec{r}, \tilde{t}') \times (\vec{n}(\vec{r}, \tilde{t}') - \vec{\beta}(\tilde{t})) \times \dot{\vec{\beta}}(\tilde{t})}{(1 - \vec{\beta}(\tilde{t}) \cdot \vec{n}(\vec{r}, \tilde{t}'))^3 \tilde{R}(\vec{r}, \tilde{t}')} \right) \Big|_{\tilde{t}'=\tilde{t}_{ret}}, \\ \vec{B}(\vec{r}, \tilde{t}) &= \left(\vec{n}(\vec{r}, \tilde{t}') \times \vec{E}(\vec{r}, \tilde{t}) \right) \Big|_{\tilde{t}'=\tilde{t}_{ret}}. \end{aligned} \tag{D.6}$$

List of Figures

1.1. Illustration of how to calculate the energy emission of a moving particle with charge q	11
1.2. Radiation characteristics of an moving charged particle	13
2.1. Procedural Error	19
2.2. Velocity space showing the rotation from \vec{v}_- to \vec{v}'	22
2.3. Determination of $ \tan(\frac{\theta}{2}) $ from boris roation	23
3.1. Interpolation of Trajectories	25
3.2. Cube with its eight corner points A, B, C, ..., H and interpolation point P_f	26
4.1. Yee-Box	29
4.2. Comparison of numerical and analytical dispersion relation of discretized Maxwell Equations with Yee Scheme	32
4.3. near fields of one and two particles	34
4.4. One plane of a grid showing the near field and far field of a particle. The near field does not contain any field values of the particle	35
4.5. Section of a grid with three boxes, two of which are near field boxes (NF) and one being a far field box (FF)	37
4.6. Simulation of an electron with $\gamma = 1.1$ in a constant $B_z = 1$ field	39
4.7. Gyration of two electrons with $\gamma = 1.1$ each.	40
4.8. Particle push from time t to $t + dt$. Since the particle changes its box the near field region also changes	41
4.9. Simulation of an electron with $\gamma = 1.2$ in a crossed electromagnetic field with $B_z = 1$ and $E_y = 0,2$	42
4.10. The faster the particle gets, the longer the history needs to be	43
4.11. Initial fields for different values of simulation parameter t	45
4.12. Flow Chart showing the relevant function calls when the user sets $t = t_0 > 0$	46
4.13. External laser pulse at $t = 700$	49
4.14. Initial Conditions: <code>Particle1->u[1] = 0.1, Particle1->u[2] = 0.01</code> and <code>Particle1->u[3] = 0.0</code>	50

LIST OF FIGURES

4.15. Ratio of the damping force g^μ and Lorentz force F_L at $\gamma = 1.0$. g^μ was calculated at each time step according to (2.3). Obviously, the damping term g^μ can be neglected. Time is in units of $e^2/(4\pi\epsilon_0 m_e c^3) = 9.40 \cdot 10^{-24}$ s.	50
4.16. Initial Conditions: Particle1->u[1] = 0.46, Particle1->u[2] = 0.01 and Particle1->u[3] = 0.0	51
4.17. Ratio of the damping force g^μ and Lorentz force F_L at $\gamma = 1.1$. g^μ was calculated at each time step according to (2.3). Obviously, the damping term g^μ can be neglected. Time is in units of $e^2/(4\pi\epsilon_0 m_e c^3) = 9.40 \cdot 10^{-24}$ s.	51
4.18. Initial Conditions: Particle1->u[1] = 0.67, Particle1->u[2] = 0.01 and Particle1->u[3] = 0.0	52
4.19. Ratio of the damping force g^μ and Lorentz force F_L at $\gamma = 1.2$. g^μ was calculated at each time step according to (2.3). Obviously, the damping term g^μ can be neglected. Time is in units of $e^2/(4\pi\epsilon_0 m_e c^3) = 9.40 \cdot 10^{-24}$ s.	52
4.20. Initial Conditions: Particle1->u[1] = 0.84, Particle1->u[2] = 0.01 and Particle1->u[3] = 0.0	53
4.21. Ratio of the damping force g^μ and Lorentz force F_L at $\gamma = 1.3$. g^μ was calculated at each time step according to (2.3). Obviously, the damping term g^μ can be neglected. Time is in units of $e^2/(4\pi\epsilon_0 m_e c^3) = 9.40 \cdot 10^{-24}$ s.	53
4.22. Initial Conditions: Particle1->u[1] = 0.98, Particle1->u[2] = 0.01 and Particle1->u[3] = 0.0	54
4.23. Ratio of the damping force g^μ and Lorentz force F_L at $\gamma = 1.4$. g^μ was calculated at each time step according to (2.3). Obviously, the damping term g^μ can be neglected. Time is in units of $e^2/(4\pi\epsilon_0 m_e c^3) = 9.40 \cdot 10^{-24}$ s.	54
4.24. Initial Conditions: Particle1->u[1] = 1.12, Particle1->u[2] = 0.01 and Particle1->u[3] = 0.0	55
4.25. Ratio of the damping force g^μ and Lorentz force F_L at $\gamma = 1.5$. g^μ was calculated at each time step according to (2.3). Obviously, the damping term g^μ can be neglected. Time is in units of $e^2/(4\pi\epsilon_0 m_e c^3) = 9.40 \cdot 10^{-24}$ s.	55
4.26. Fourier analysis of the electric field components of \vec{E} at $\gamma = 1.0$	56
4.27. Fourier analysis of the components of the Poynting vector \vec{S} at $\gamma = 1.0$. . .	57
4.28. Fourier analysis of the electric field components of \vec{E} at $\gamma = 1.1$	57
4.29. Fourier analysis of the components of the Poynting vector \vec{S} at $\gamma = 1.1$. . .	58
4.30. Fourier analysis of the electric field components of \vec{E} at $\gamma = 1.2$	58
4.31. Fourier analysis of the components of the Poynting vector \vec{S} at $\gamma = 1.2$. . .	59
4.32. Fourier analysis of the electric field components of \vec{E} at $\gamma = 1.3$	59
4.33. Fourier analysis of the components of the Poynting vector \vec{S} at $\gamma = 1.3$. . .	60
4.34. Fourier analysis of the electric field components of \vec{E} at $\gamma = 1.4$	60

LIST OF FIGURES

4.35. Fourier analysis of the components of the Poynting vector \vec{S} at $\gamma = 1.4$	61
4.36. Fourier analysis of the electric field components of \vec{E} at $\gamma = 1.5$	61
4.37. Fourier analysis of the components of the Poynting vector \vec{S} at $\gamma = 1.5$	62
5.1. Wave with wavevector \vec{k} , arbitrary polarization and angle of incidence θ at a surface with impedance η_i and refractive index n_i	66
5.2. Simulation using UPML	71

Bibliography

- [1] Klassische elektrodynamik. von j. d. jackson. 2., $\tilde{A}^{\frac{1}{4}}$ berarbeitete auflage 1975, $\tilde{A}^{\frac{1}{4}}$ ersetzt von k. muller, 1020 seiten, einige abbildungen, walter de gruyter verlag berlin, new york 1981, dm 98,-. *Physik in unserer Zeit*, 13(2):64–64, 1982.
- [2] J. Barnes and P. Hut. A hierarchical $O(N \log N)$ force-calculation algorithm. *nature*, 324:446–449, December 1986.
- [3] Jean-Pierre Berenger. A perfectly matched layer for the absorption of electromagnetic waves. *J. Comput. Phys.*, 114(2):185–200, October 1994.
- [4] M. Bonitz and D. Semkat. *Introduction to Computational Methods in Many Body Physics*. Rinton Press, 2006.
- [5] J. P. Boris. Relativistic plasma simulation-optimization of a hybrid code. *Proceeding of Fourth Conference on Numerical Simulations of Plasmas*, November 1970.
- [6] A.Bruce Langdon Charles K. Birdsall. *Plasma physics via computer simulation*. IOP, 1991.
- [7] Weng Cho Chew and William H. Weedon. A 3-d perfectly matched medium from modified maxwell's equations with stretched coordinates. *Microwave Opt. Tech. Lett*, 7:599–604, 1994.
- [8] B. I. Cohen, M. A. Mostrom, D. R. Nicholson, A. N. Kaufman, C. E. Max, and A. B. Langdon. Simulation of laser beat heating of a plasma. *Physics of Fluids*, 18:470–474, April 1975.
- [9] John M. Dawson. Particle simulation of plasmas. *Rev. Mod. Phys.*, 55:403–447, Apr 1983.
- [10] P. A. M. Dirac. The quantum theory of the electron. *Proceedings of the Royal Society of London A: Mathematical, Physical and Engineering Sciences*, 117(778):610–624, 1928.

BIBLIOGRAPHY

- [11] R. A. Fonseca, L. O. Silva, F. S. Tsung, V. K. Decyk, W. Lu, C. Ren, W. B. Mori, S. Deng, S. Lee, T. Katsouleas, and J. C. Adam. *OSIRIS: A Three-Dimensional, Fully Relativistic Particle in Cell Code for Modeling Plasma Based Accelerators*. Springer Berlin Heidelberg, Berlin, Heidelberg, 2002.
- [12] C. Herzing. *Die molekulardynamische Simulation strahlender Plasmen*. PhD thesis, Ludwig Maximilians Universität München, Lehrstuhl für Plasma & Computational Physics, 2016.
- [13] Christian Kanzow. *Numerische Mathematik II*. 2005. [Online; accessed 13-Oktober-2016].
- [14] E.M.Lifschitz L.D.Landau. *Lehrbuch der klassischen Physik*, volume 2 of *Klassische Feldtheorie*. Harri (Deutsch), 12 edition, 1997.
- [15] W. Nolting. *Grundkurs Theoretische Physik 3*: Grundkurs Theoretische Physik / Wolfgang Nolting. Springer, 2004.
- [16] A. Pukhov. Three-dimensional electromagnetic relativistic particle-in-cell code VLPL (Virtual Laser Plasma Lab). *Journal of Plasma Physics*, 61(03):425–433, April 1999.
- [17] C. M. Rappaport. Perfectly matched absorbing boundary conditions based on anisotropic lossy mapping of space. *IEEE Microwave and Guided Wave Letters*, 5(3):90–92, Mar 1995.
- [18] Chuang Ren. *Introduction to Particle-in-Cell Methods in Plasma Simulations*. 2011. [Online; accessed 14-Mai-2017].
- [19] Raymond Rumpf. Electromagnetic analysis using finite-difference time-domain. University Lecture, 2014.
- [20] A. Taflove and S.C. Hagness. *Computational Electrodynamics: The Finite-difference Time-domain Method*. Artech House antennas and propagation library. Artech House, 2005.
- [21] F. L. Teixeira and W. C. Chew. General closed-form pml constitutive tensors to match arbitrary bianisotropic and dispersive linear media. *IEEE Microwave and Guided Wave Letters*, 8(6):223–225, Jun 1998.

BIBLIOGRAPHY

- [22] Kane S. Yee. Numerical solution of initial boundary value problems involving maxwell's equations in isotropic media. *IEEE Trans. Antennas and Propagation*, pages 302–307, 1966.

Declaration

Erklärung:

Hiermit erkläre ich, die vorliegende Arbeit selbständig verfasst zu haben und keine anderen als die in der Arbeit angegebenen Quellen und Hilfsmittel benutzt zu haben.

München, Datum der Abgabe

München, 18.07.2017, David Symhoven